

The CARMENES search for exoplanets around M dwarfs

A sub-Neptunian mass planet in the habitable zone of HN Lib

E. González-Álvarez^{1,2*}, J. Kemmer^{3*}, P. Chaturvedi⁴, J. A. Caballero¹, A. Quirrenbach³, P. J. Amado⁵, V. J. S. Béjar^{6,7}, C. Cifuentes¹, E. Herrero⁹, D. Kossakowski¹⁰, A. Reiners¹¹, I. Ribas^{8,9}, E. Rodríguez⁵, C. Rodríguez-López⁵, J. Sanz-Forcada¹, Y. Shan^{12,11}, S. Stock³, H. M. Tabernero¹, L. Tal-Or^{13,11}, M. R. Zapatero Osorio¹, A. P. Hatzes⁴, Th. Henning¹⁰, M. J. López-González⁵, D. Montes², J. C. Morales^{8,9}, E. Pallé^{6,7}, S. Pedraz¹⁴, M. Perger^{8,9}, S. Reffert³, S. Sabotta³, A. Schweitzer¹⁵, and M. Zechmeister¹¹

¹ Centro de Astrobiología, CSIC-INTA, Carretera de Ajalvir km 4, 28850 Torrejón de Ardoz, Madrid, Spain

² Departamento de Física de la Tierra y Astrofísica & IPARCOS-UCM (Instituto de Física de Partículas y del Cosmos de la UCM), Facultad de Ciencias Físicas, Universidad Complutense de Madrid, 28040 Madrid, Spain

³ Landessternwarte, Zentrum für Astronomie der Universität Heidelberg, Königstuhl 12, 69117 Heidelberg, Germany

⁴ Thüringer Landessternwarte Tautenburg, Sternwarte 5, D-07778 Tautenburg, Germany

⁵ Instituto de Astrofísica de Andalucía (IAA-CSIC), Glorieta de la Astronomía s/n, 18008 Granada, Spain

⁶ Instituto de Astrofísica de Canarias, Avenida Vía Láctea s/n, E-38205 La Laguna, Tenerife, Spain

⁷ Departamento de Astrofísica, Universidad de La Laguna, E-38206 La Laguna, Tenerife, Spain

⁸ Institut de Ciències de l'Espai (IEEC-CSIC), Campus UAB, Carrer de Can Magrans s/n, 08193, Bellaterra, Spain

⁹ Institut d'Estudis Espacials de Catalunya (IEEC), E-08034 Barcelona, Spain

¹⁰ Max-Planck-Institut für Astronomie, Königstuhl 17, 69117 Heidelberg, Germany

¹¹ Institut für Astrophysik, Georg-August-Universität, Friedrich-Hund-Platz 1, 37077 Göttingen, Germany

¹² Centre for Earth Evolution and Dynamics, Department of Geosciences, Universitetet i Oslo, Sem Sælands vei 2b, 0315 Oslo, Norway

¹³ Department of Physics, Ariel University, Ariel, 40700, Israel

¹⁴ Centro Astronómico Hispano en Andalucía, Observatorio de Calar Alto, Sierra de los Filabres, 04550 Gérgal, Spain

¹⁵ Hamburger Sternwarte, Gojenbergsweg 112, 21029 Hamburg, Germany

Received 28 February 2023 / Accepted 11 May 2023

ABSTRACT

We report the discovery of HN Lib b, a sub-Neptunian mass planet orbiting the nearby ($d \approx 6.25$ pc) M4.0 V star HN Lib detected by our CARMENES radial-velocity (RV) survey. We determined a planetary minimum mass of $M_b \sin i = 5.46 \pm 0.75 M_\oplus$ and an orbital period of $P_b = 36.116 \pm 0.029$ d, using ~ 5 yr of CARMENES data, as well as archival RVs from HARPS and HIRES spanning more than 13 years. The flux received by the planet equals half the insolation on Earth, which places it in the middle of the conservative habitable zone (HZ) of its host star. The RV data show evidence for another planet candidate with $M_{[c]} \sin i = 9.7 \pm 1.9 M_\oplus$ and $P_{[c]} = 113.46 \pm 0.20$ d. The long-term stability of the signal and the fact that the best model for our data is a two-planet model with an independent activity component stand as strong arguments for establishing a planetary origin. However, we cannot rule out stellar activity due to its proximity to the rotation period of HN Lib, which we measured using CARMENES activity indicators and photometric data from a ground-based multi-site campaign as well as archival data. The discovery adds HN Lib b to the shortlist of super-Earth planets in the habitable zone of M dwarfs, but HN Lib [c] probably cannot be inhabited because, if confirmed, it would most likely be an icy giant.

Key words. techniques: photometric – techniques: radial velocities – stars: individual: HN Lib – stars: late-type – stars: planetary systems

1. Introduction

In the last decade, spectrographs delivering high-precision radial velocity (RV) measurements have reached the necessary precision to detect small planets close to (and even within) the habitable zone (HZ; e.g., [Kasting et al. 1993](#); [Kopparapu et al. 2014](#)) of late-type main-sequence stars. The predicted high number of super-Earth and Earth-like planets in the HZ that could be detected around M-dwarf stars makes these stars extremely inter-

esting objects for planetary RV searches ([Udry et al. 2007](#); [Zechmeister et al. 2009](#); [Dressing & Charbonneau 2013](#); [Bonfils et al. 2013](#); [Tuomi et al. 2014](#); [Sabotta et al. 2021](#)). Despite the significant number of detected planets around M-dwarf primaries, we are still far from fully understanding fundamental questions, such as how these planetary systems form and evolve ([Ida & Lin 2005](#); [Raymond et al. 2007](#); [Burn et al. 2021](#); [Schlecker et al. 2022](#)). Especially for the planets in the HZ, the formation history is important. This is because not only is the incoming stellar flux a crucial component in determining the actual habitability, but so are the properties of the planet itself, such as the composition of a potential atmosphere ([Tarter et al. 2007](#); [Kaltenegger 2017](#)).

Send offprint requests to: Esther González-Álvarez and Jonas Kemmer
e-mail: estgon11@ucm.es, jkemmer@lsw.uni-heidelberg.de

* Both authors contributed equally to the manuscript.

In this context, the increasing number of M-dwarf stars that harbor planets in the HZ (e.g., Suárez Mascareño et al. 2023 and Kossakowski et al. 2023, to cite the two most recent examples based on the radial velocity method) plays a significant role in exploring theories of planet formation and evolution.

Here, we present the discovery of a sub-Neptunian mass planet orbiting in the HZ of the nearby mid-M dwarf HNLiB. The planet’s orbital parameters are derived from an RV model that includes Keplerian orbits for the planet and another planet candidate, as well as a red-noise model driven by a Gaussian process (GP) to simultaneously account for the stellar activity.

In Sect. 2, we present the analyzed ground-based observations. The properties of the host star, HNLiB, are introduced in Sect. 3. The stellar activity analysis and the determination of the rotation period of the parent star are carried out in Sect. 4. Also in this section, with the stellar rotation period constrained, we proceed to analyze the spectroscopic observations with the aim of identifying and characterizing planet candidates. The properties of the newly confirmed and discovered planet and the planet candidate orbiting HNLiB are given in Sect. 5, together with the discussion on the implications of these findings. Finally, a summary is given in Sect. 6.

2. Observations

2.1. Spectroscopic data

2.1.1. CARMENES

HNLiB was spectroscopically observed with CARMENES between 27 January 2016 and 31 December 2020, resulting in a total of 94 RV measurements. CARMENES is installed at the 3.5 m telescope of the Calar Alto Observatory in Almería (Spain). It was specifically designed to deliver high-resolution spectra at optical (resolving power $\mathcal{R} \approx 94,600$) and near-infrared ($\mathcal{R} \approx 80,400$) wavelengths covering the range from 520 nm to 1710 nm. CARMENES has two different channels, one for the optical (the VIS channel) and one for the near-infrared (the NIR channel) with a dichroic at 960 nm (Quirrenbach et al. 2014). All data were acquired with integration times of 1800 s, which is the maximum exposure time employed for precise RV measurements with CARMENES.

The spectra were processed following the data flow of the CARMENES guaranteed time observations (GTO) program (Ribas et al. 2023). Raw data are reduced with the caracal pipeline (Caballero et al. 2016a). Relative RVs are extracted separately for the VIS and NIR channels using the *serval* software (Zechmeister et al. 2018). The final RV per epoch of each channel is computed as the weighted RV mean over all échelle orders. The data from the CARMENES VIS channel are shown in the bottom panel of Fig. 1 (individual CARMENES relative RVs and their uncertainties are listed in Table C.1). The root mean square (rms) from the final fit residuals and the mean errorbars of the CARMENES RV data are 1.75 m s^{-1} and 1.31 m s^{-1} , respectively.

At high spectral resolution, the profile of the stellar lines may change due to photospheric and chromospheric activity, which has an impact on accurate RV measurements. Therefore, for CARMENES, *serval* provides further measurements for a number of spectral features in the instruments’ wavelength range that are considered indicators of stellar activity and may have a chromospheric component in active M dwarfs: the differential line width (dLW), the Ca II infrared triplet, H α , and the chromatic index (CRX). The latter determines the RV–log λ correla-

tion, and it is used as an indicator for the presence of stellar active regions. Additionally, as part of the data processing, we also calculate measurements of molecular absorption bands of two species: TiO and VO, together with pseudo-equivalent widths (pEW) for different indices after the subtraction of a reference star spectrum as described by Schöfer et al. (2019). An overview of the CARMENES activity indicators of HNLiB that exhibit significant peaks in the generalized Lomb-Scargle periodograms (GLS; Zechmeister & Kürster 2009) is shown in Fig. 2.

2.1.2. Archival data

Additional relative RV data for HNLiB are available in the archives. We employed 14 RVs (Trifonov et al. 2020) from the High Accuracy Radial velocity Planet Searcher (HARPS, Mayor et al. 2003) at the ESO La Silla 3.6 m telescope and 34 RV data (Tal-Or et al. 2019) from the High Resolution Echelle Spectrometer (HIRES, Vogt et al. 1994) on the Keck 10 m telescope. These velocities span a period of ~ 9 yr, almost doubling the total time coverage of our RV analysis. The mean error bars are 1.47 m s^{-1} for the HARPS data and 2.83 m s^{-1} for HIRES.

2.2. Ground-based photometry

There are data from many photometric monitoring campaigns of HNLiB available. An overview of the data used in this work and their properties can be found in Table 1.

2.2.1. OSN and TJO

HNLiB was observed by our team using the 90 cm Ritchey-Chrétien telescope of the Observatorio de Sierra Nevada (OSN) in Almería, Spain, and the VersArray $2k \times 2k$ CCD camera (Rodríguez et al. 2010). The total number of frames amounts to 915 in the *V* filter and 903 in the *R* filter, where the typical exposure times were 100 s and 60 s, respectively. Each filter dataset was corrected for bias and flat fielding before the target flux was determined using differential aperture photometry. Outliers differing by more than 3σ from the mean were removed from further analysis. The nightly binned light curves are presented in the first two panels of Fig. 3.

Further photometric CCD observations were collected by us with the 0.8 m Telescopi Joan Oró (TJO, Colomé et al. 2010) at the Observatori Astronòmic del Montsec in Lleida, Spain. A total of 1910 frames with a exposure time of 25 s were obtained using the Johnson *R* filter of the LAIA imager, a $4k \times 4k$ CCD with a field of view of 30 arcmin, and a scale of $0.4 \text{ arcsec pixel}^{-1}$. The images were calibrated with bias, dark, and flat-field frames with the ICAT pipeline (Colomé & Ribas 2006) of the TJO. The differential photometry was extracted with AstroImageJ (Collins et al. 2017) using the aperture size that minimized the rms of the resulting relative fluxes, and a selection of the 30 brightest comparison stars in the field that did not show variability. Lastly, we removed outliers and measurements affected by poor observing conditions with a low signal-to-noise ratio. The nightly binned TJO *R*-band light curve is presented in the middle panel of Fig. 3.

2.2.2. Archival data

Photometric public data of HNLiB were also used for the analysis. We retrieved archival data from the MEarth project (Irwin et al. 2015, DR 11¹ – last two panels of Fig. 3), the All-Sky

¹ <https://lweb.cfa.harvard.edu/MEarth/DR11/README.txt>

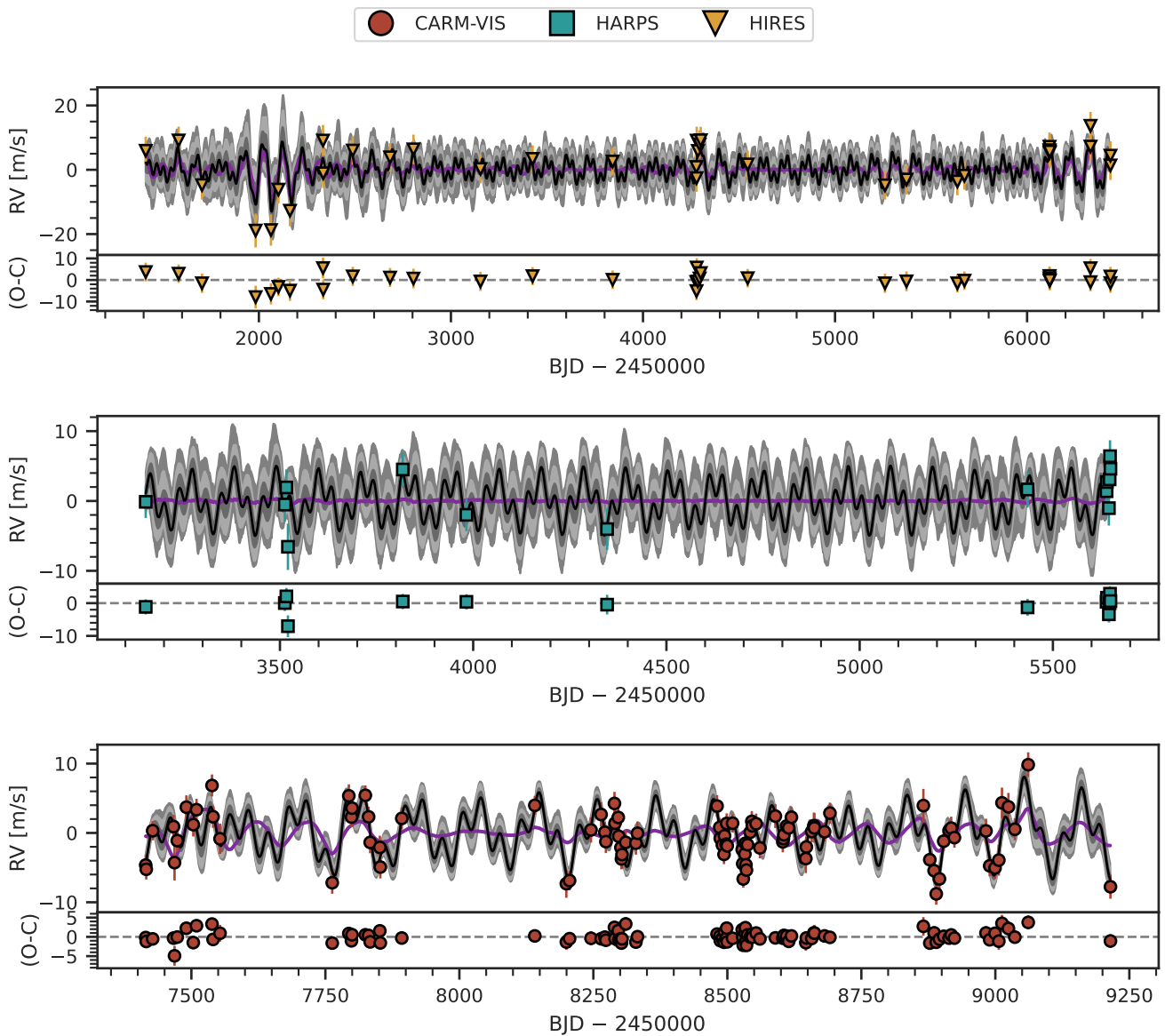


Fig. 1. RVs of HN Lib over time. The red, green, and yellow markers depict the CARMENES VIS, HARPS, and HIRES RV data, respectively. The black lines show the median of 10 000 samples from the posterior of the final $2P_{(36\text{d-ecc}, 113\text{d-circ})} + \text{dSHO-GP}_{(96\text{d})}$ model. Grey shaded areas denote the 68 %, 95 %, and 99 % confidence intervals, respectively. The purple line shows the GP part of the model. The instrumental RV offsets were subtracted from the measurements and the models. Error bars of the measurements include the jitter added in quadrature. The residuals after subtracting the median models are shown in the lower panels of each plot.

Automated Survey (ASAS-3, [Pojmanski 1997](#)), the Wide Angle Search for Planets (SuperWASP, [Pollacco et al. 2006](#)), and the All-Sky Automated Survey for Supernovae project (ASAS-SN, [Shappee et al. 2014](#); [Kochanek et al. 2017](#)). [Díez Alonso et al. \(2019\)](#) searched for rotation periods using the ASAS-3 photometric data but did not report a detection for HN Lib. To reach a higher precision for our analysis, we created nightly bins of the data from each instrument if multiple data points were taken per night.

Since the quality of the light curves of ASAS-3 and ASAS-SN is considerably worse than that of the others (cf. [Table 1](#)), we did not use them for our final analysis. For the MEarth data, we considered a photometric offset for each version of the respective instruments since they go along with the creation of a new per-star magnitude and meridian offset for the data ([Newton et al. 2018](#)). Some resulting sub-data sets have only a few data points

and are not very useful due to the ambiguous offset in the fit, which is why we did not consider them in the final analysis (see also [Table 1](#)).

3. HN Lib

HN Lib is a nearby, single M4.0 V star located at a distance of only about 6.25 pc ([Gaia Collaboration et al. 2022](#)). Because of its relative brightness, this star has often appeared in the literature and in all-sky surveys (e.g. [Schönfeld 1886](#); [Jackson & Turner 1952](#); [Leggett 1992](#); [Mann et al. 2015](#)). [Table 2](#) summarises its stellar parameters.

HN Lib is cataloged as a variable star that exhibits variations in its luminosity due to rotation of the star coupled with star spots and other chromospheric activity ([Kukarkin & Kholopov 1982](#); [Weis 1994](#); [Hosey et al. 2015](#)). Furthermore, [Astudillo-](#)

Table 1. Available long-term photometric observations of HN Lib.

Instrument	Date		Filter	Δt^a [d]	N_{obs}^b	rms ^c [ppt]
	Begin	End				
ASAS-3 [†]	24 December 2000	13 September 2009	V	3185	446	24.60
SuperWASP [†]	28 February 2010	26 July 2010	400–700 nm	147	86	3.23
ASAS-SN [†]	27 February 2012	10 July 2018	V	2324	97	23.29
	22 June 2013	23 May 2018		1796	111	19.46
	25 June 2014	28 August 2018		1525	115	40.24
	10 July 2014	28 August 2018		1510	129	15.96
MEarth-tel14	28 May 2017 [†]	9 June 2017 [†]	RG715	11	8	3.72
	1 July 2017 [†]	8 July 2017 [†]		6	4	5.32
	28 August 2017 [†]	8 September 2017 [†]		10	11	4.33
	4 June 2019	27 February 2022		999	265	4.80
MEarth-tel15	11 June 2017 [†]	21 June 2017 [†]	RG715	9	7	2.46
	30 June 2017 [†]	30 June 2017 [†]		0	1	0.98
	13 July 2019	16 March 2020		246	70	4.10
OSN-T90	10 May 2018	5 June 2019	R	391	49	8.68
	10 May 2018	5 June 2019	V	391	48	9.00
TJO	9 January 2019	9 March 2020	R	424	102	8.44

Notes. ^(a) Time-span of the observations. ^(b) Binned nightly. ^(c) Root mean square in parts-per-thousand. Data sets that were not used for the photometric rotational period determination are indicated by a dagger †.

Defru et al. (2017) determined a $\log R'_{\text{HK}}$ value for HN Lib of -5.58 ± 0.05 dex and estimated from activity-rotation relationships a stellar rotation period of 102 ± 11 d, which classifies our target as a slow rotator. This conclusion is in line with the small upper limits of rotational velocity, magnetic field, and X-ray luminosity (Stelzer et al. 2013; Reiners et al. 2018, 2022), a new, more robust, mean $\log R'_{\text{HK}}$ value of -5.23 ± 0.07 dex homogeneously computed by averaging individual values collected with HARPS, FEROS, HIRES, and ESPaDONS (Perdelwitz et al. 2021), the measurement of chromospheric lines in absorption or moderate emission (Fuhrmeister et al. 2020), and our own rotation period determination (see below).

The fundamental atmospheric parameters (i.e., T_{eff} , $\log g$, and [Fe/H]) of HN Lib using the CARMENES VIS and NIR template spectra were recently determined by Marfil et al. (2021) by means of the STEPARSYN code² (Tabernero et al. 2022). The resulting values, listed in Table 2, agree at the 2σ level with those derived by other authors via spectral synthesis (e.g. Rojas-Ayala et al. 2012; Gaidos et al. 2015; Passegger et al. 2018; Rajpurohit et al. 2018; Maldonado et al. 2020) and from fits to the photometric spectral energy distribution (Cifuentes et al. 2020).

We followed the recipes of the latter authors to determine a new bolometric luminosity, L_{\star} , with updated *Gaia* DR3 data. We used L_{\star} and T_{eff} to determine the mass and radius of HN Lib to be $M_{\star} = 0.291 \pm 0.014 M_{\odot}$ and $R_{\star} = 0.299 \pm 0.009 R_{\odot}$ with Stefan–Boltzmann law and the mass-radius relation of Schweitzer et al. (2019), which was based on detached, double-lined, double-eclipsing, main-sequence M-dwarf binaries from the literature.

Besides, we employed the spectral synthesis method, together with the PHOENIX BT-Settl atmospheric models (Allard et al. 2012) and the radiative transfer code Turbospectrum (Plez 2012) for determining Mg and Si abundances of HN Lib. We measured [Mg/H] = -0.16 ± 0.14 dex and [Si/H] = $0.06 \pm$

0.20 dex. Further details on the followed procedure will be provided by Tabernero et al. (in prep.).

The galactic space velocities UVW of HN Lib were derived using the *Gaia* DR3 coordinates, proper motions, and systemic radial velocity with the formulation developed by Johnson & Soderblom (1987).

HN Lib does not appear to belong to any known young stellar moving group and has kinematics typical of a stars in the galactic thin disk, indicating a likely age of 0.8–8.0 Gyr, which is in agreement with the very weak stellar activity. The proximity of HN Lib has made our target to be the subject of numerous searches for close companions (e.g., Jameson et al. 1983; Skrutskie et al. 1989; Nakajima et al. 1994; Simons et al. 1996; Oppenheimer et al. 2001; Hinz et al. 2002; Tanner et al. 2010; Jódar et al. 2013; Ward-Duong et al. 2015; Davison et al. 2015; Cortés-Contreras et al. 2017). The high-resolution images of Dieterich et al. (2012) were the most sensitive to very-low-mass stars, brown dwarfs, or planets using NICMOS on the *Hubble* with the F180M near-infrared filter. Dieterich et al. (2012) established companion magnitude and angular separation limits ranging from 11.5 mag at 0.4 arcsec (2.5 au) to 18 mag at 3.0–4.0 arcsec (19–25 au) for companions that could be ruled out for HN Lib. These limits, together with the age of the system and the evolutionary models for very-low-mass stars and brown dwarfs with dusty atmospheres from Baraffe et al. (2015), discard any hypothetical companion with mass from 0.07 to 0.08 M_{\odot} at projected orbital separations larger than 0.4 arcsec, and from 0.025 to 0.06 M_{\odot} at separations larger than 3.0–4.0 arcsec. Finally, as in (Caballero et al. 2022), we searched for objects with common *Gaia* DR3 parallax and proper motions up to a projected physical separation of 100 000 au. We found no hints of any wide potential companion.

² <https://github.com/hmtabernero/SteParSyn/>

Table 2. Stellar parameters of HN Lib.

Parameter	Value	Reference
<i>Basic identifiers and data</i>		
BD	−11 3759	Scho86
Wolf	1481	Wol25
Gl	555	Gli69
Karmn	J14342−125	AF15, Cab16b
Sp. type	M4.0 V	Haw96
G [mag]	9.8950 ± 0.0030	<i>Gaia</i> DR3 ^a
J [mag]	6.838 ± 0.019	2MASS ^a
<i>Astrometry and kinematics</i>		
α (ICRS, epoch 2016.0)	14:34:16.424	<i>Gaia</i> DR3
δ (ICRS, epoch 2016.0)	−12:31:00.92	<i>Gaia</i> DR3
$\mu_\alpha \cos \delta$ [mas yr ^{−1}]	$−355.138 \pm 0.053$	<i>Gaia</i> DR3
μ_δ [mas yr ^{−1}]	$+593.040 \pm 0.044$	<i>Gaia</i> DR3
ϖ [mas]	159.923 ± 0.055	<i>Gaia</i> DR3
d [pc]	6.2530 ± 0.0022	<i>Gaia</i> DR3
γ [km s ^{−1}]	$−1.426 \pm 0.006$	Sou18
$\dot{\gamma}$ [m s ^{−1} yr ^{−1}]	$+0.06901 \pm 0.00041$	This work
U [km s ^{−1}]	$−13.8606 \pm 0.0051$	This work
V [km s ^{−1}]	$+5.8821 \pm 0.0053$	This work
W [km s ^{−1}]	$+13.9700 \pm 0.057$	This work
Galactic population	Thin disk	This work
<i>Fundamental parameters and abundances</i>		
T_{eff} [K]	3347 ± 50	Mar21
$\log g$	4.76 ± 0.13	Mar21
[Fe/H]	$−0.18 \pm 0.15$	Mar21
[Mg/H]	$−0.16 \pm 0.14$	Tab
[Si/H]	$+0.06 \pm 0.20$	Tab
L_\star [$10^{-6} L_\odot$]	10106 ± 69	This work
R_\star [R_\odot]	0.299 ± 0.009	This work
M_\star [M_\odot]	0.291 ± 0.013	This work
<i>Activity and age</i>		
$v \sin i_\star$ [km s ^{−1}]	< 2.0	Rei18
P_{rot} [d]	96 ± 2	This work
pEW(He I D ₃) [Å]	$+0.070 \pm 0.010$	Fuh20
pEW(H α) [Å]	$+0.088 \pm 0.037$	Fuh20
pEW(Ca II IRT ₁) [Å]	$−0.006 \pm 0.015$	Fuh20
pEW(He I IR) [Å]	$+0.498 \pm 0.004$	Fuh20
$\log R'_{\text{HK}}$	$−5.226^{+0.063}_{−0.074}$	This work ^b
$\langle B \rangle$ [G]	< 220	Rei22
$\log L_X$ [erg s ^{−1}]	< 26.80	This work ^c
Age [Gyr]	0.8–8.0	This work

References. 2MASS: Skrutskie et al. (2006); AF15: Alonso-Floriano et al. (2015); Cab16b: Caballero et al. (2016b); Fuh20: Fuhrmeister et al. (2020); *Gaia* DR3: Gaia Collaboration et al. (2021); Gli69: Gliese (1969); Mar21: Marfil et al. (2021); Haw96: Hawley et al. (1996); Rei18: Reiners et al. (2018); Rei22: Reiners et al. (2022); Scho86: Schönfeld (1886); Ste13: Stelzer et al. (2013); Sou18: Soubiran et al. (2018); Tab: Tabernero et al. (in prep.); Wol25: Wolf (1925).

Notes. ^(a) See Cifuentes et al. (2020) for multiband photometry different from *Gaia* G and 2MASS J . ^(b) From data compiled by Perdelwitz et al. (2021). ^(c) Computed by us from a $\log f_X$ upper limit by Stelzer et al. (2013).

4. Analysis and results

4.1. Modeling techniques

To get a quick overview of all the different data available to us, we used the graphical user interface capabilities of

Table 3. Derived stellar rotation period values using various methods.

Method	Value
$\log R'_{\text{HK}}^{(a)}$	102 ± 11 d
Spectral act. indicators ^(b)	94 and 125 d
Phot. QP-GP kernel	94 ± 4 d
Phot. dSHO-GP kernel	96 ± 2 d

Notes. ^(a) Astudillo-Defru et al. (2017). ^(b) These values are aliases one of each other.

Exo-Striker³ (Trifonov 2019) to generate GLS periodograms of RVs, photometry, and spectral activity indicators. For the retrieval of the parameters presented in the final analysis of this work, we used however the juliet⁴ package (Espinoza et al. 2019) because of the variety of GP regression kernels that it provides. It brings together frequently used tools such as radvel (Fulton et al. 2018) for RV modeling and celerite (Foreman-Mackey et al. 2017) and george (Ambikasaran et al. 2015) for the implementation of GPs. For the fitting process, juliet offers different options. We chose to use dynesty (Speagle 2020), which implements a nested sampling algorithm and supports computing Bayesian log evidence, $\ln \mathcal{Z}$, for the models.

4.2. Stellar activity and rotation period

4.2.1. Activity indicators

To identify signals that originate from stellar activity, we investigated the GLS periodograms for the range of activity indicators determined from the CARMENES VIS and NIR spectra as described in Sect. 2.1. Since our observations span several years, many of the periodograms suffer from strong signals with periods of 360 d to 380 d, as well as approximately half a year, caused by uncorrected contamination by telluric lines. For those spectroscopic activity indicators that show peaks at these periodicities, we proceeded with periodograms that were pre-whitened by subtracting the best matching solution to these signals from the data. For clarity, we show only the periodograms for the activity indicators with peaks of less than 10% false alarm probability (FAP) after the pre-whitening in Fig. 2. All shown indicators share a pair of signals with periods of ~ 125 d and ~ 94 d that are caused by aliasing due to the seasonal observability of HN Lib⁵. Both periods are close to the estimate of $P_{\text{rot,est}} = 102 \pm 11$ d based on the $\log R'_{\text{HK}}$ measurement by Astudillo-Defru et al. (2017), which suggests that the underlying signal is indeed related to the stellar rotation. However, since both signals are within the tolerance of the predicted rotation period, we could not resolve the aliasing with the spectroscopic data.

4.2.2. Photometry

The GLS periodogram of the TJO photometric time series in Fig. 2 shows a peak at 95 d, with aliases at 74 d and 135 d due

³ <https://github.com/3fon3fonov/exostriker>

⁴ <https://juliet.readthedocs.io/en/latest/index.html>

⁵ The seasonal observability imprints a signal of about $1/365 \text{ d}^{-1}$ to the window function of the data. Aliasing occurs at $f_a = f_i \pm m \times f_s$, where f_a are the alias frequencies, f_i is the true underlying signal, m is an integer value and f_s is the sampling frequency. Given a signal of ~ 125 d, we therefore expect first-order aliasing at $f_a = 1/125 \text{ d} + 1/365 \text{ d} \approx 1/93 \text{ d}$.

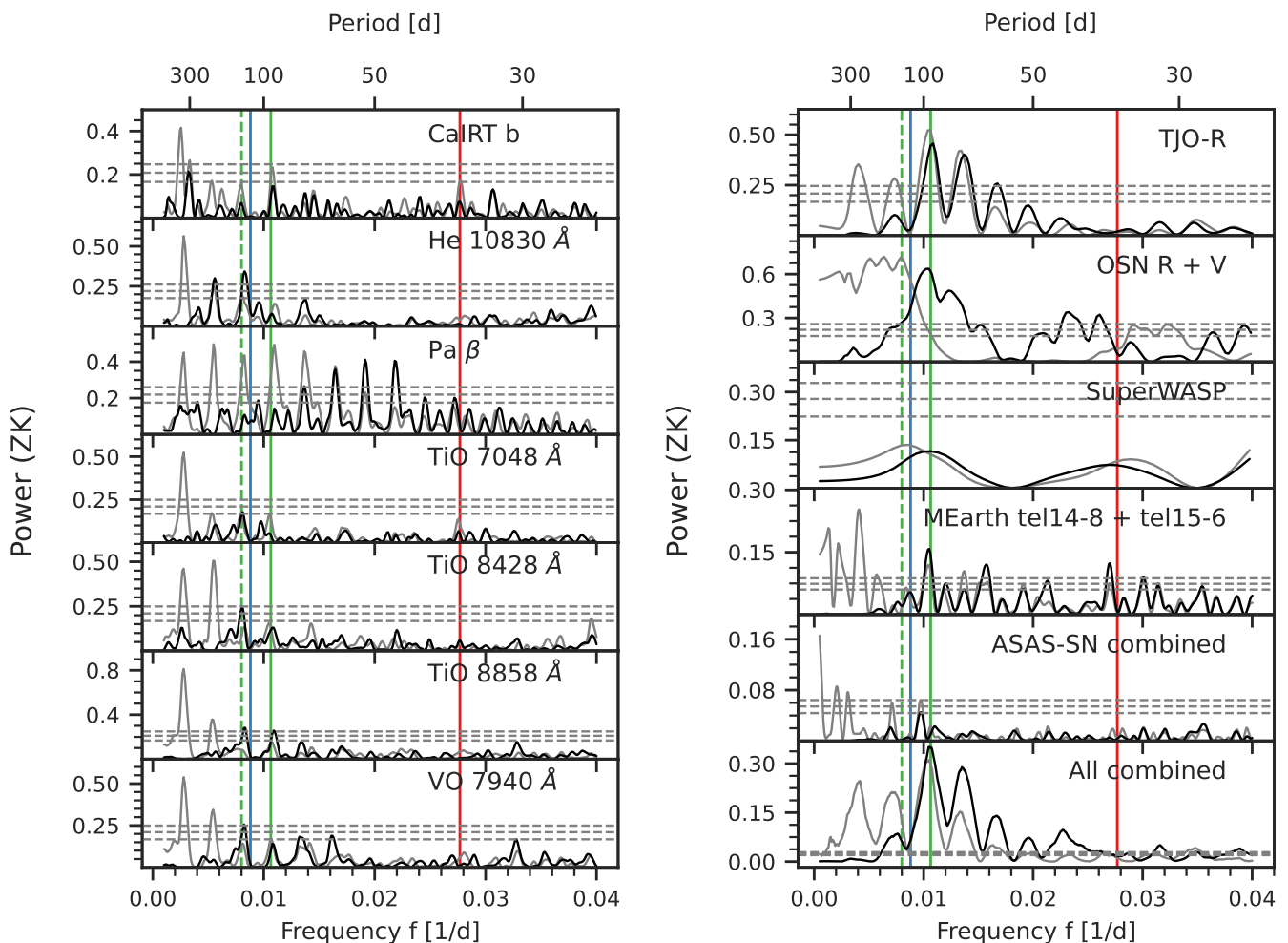


Fig. 2. Signal search with GLS periodograms in the spectral activity indicators (*left*) and photometric data (*right*) of HNLlib. The data of the activity indicators were pre-whitened by subtracting the long-period ~ 360 d or ~ 180 d signals accordingly, whereas the photometric data were detrended using CFAM to remove the appearing long-term trends. Original periodograms are shown in grey and the corrected ones in black. We mark the 36-day signal from the RVs with a red solid line and the 113-day period with a blue solid line. The common alias pair of the activity indicators with periods of ~ 125 d and ~ 94 d are depicted by green dashed and solid lines, respectively. FAPs of 10, 1, and 0.1 % were calculated with the analytical expression of Zechmeister & Kürster (2009) and are shown with the horizontal grey dashed lines from bottom to top.

to the seasonal observations. Furthermore, a long periodic signal with a period of 263 d is visible, that could be an alias of a longer activity cycle of the star. Because of the data gap of about ~ 200 d (and the consequently uncertain offset) between the two OSN observing runs and the short baseline of each data chunk, the GLS periodogram of the OSN data shows a large plateau for long periods. However, when inspected visually, the OSN and TJO photometric times series pretty much overlap (see Fig. A.4 for comparison). A periodicity of ≥ 100 d is also apparent in the periodogram of the daily binned data from the SuperWASP survey; however, despite being the most prominent peak, it is not significant in the GLS. A signal of an unknown origin at a period of 247 d is dominant in the MEarth data. In the regime of around 100 d, the strongest peak appears at 96 d, which is consistent with the TJO data.

Based on the $\log R'_{\text{HK}}$ measurements and the GLS analysis of the activity indicators, we expected the rotation period to be in the range between 90 and 130 days. Consequently, we detrended the data before further analysis due to the appearing long-term trends. For this, we used wotan (Hippke et al. 2019) and Cosine Filtering with Autocorrelation Minimization (CFAM – Kip-

ping et al. 2013; Rodenbeck et al. 2018), where we set the window length to 200 d. The CFAM had a particularly strong effect on the OSN data, as it removed the offset between the two observing seasons. Overall, the detrended photometric data share a common periodicity, which appears as a very significant signal in the combined GLS periodogram at a period of 97 d, with yearly aliases of first and second order on both sides.

To measure the photometric rotation period of HNLlib considering all photometric data combined, we used GP modeling. In contrast to the GLS periodograms, which are based on static sinusoidal models, GPs are able to represent also the quasi-periodic nature of stellar activity. For our purposes, we used two different kernels. The first one was a kernel that is the sum of two simple harmonic oscillators, in the following abbreviated as “dSHO” kernel (e.g. David et al. 2019; Gillen et al. 2020). A description of the implementation and parametrization of this kernel in juliet can be found in Kossakowski et al. (2021). The second kernel was the multiplication of an exponential-sine-squared kernel with a squared-exponential kernel, which is usually called the “quasi-periodic” (QP) kernel (Haywood et al.

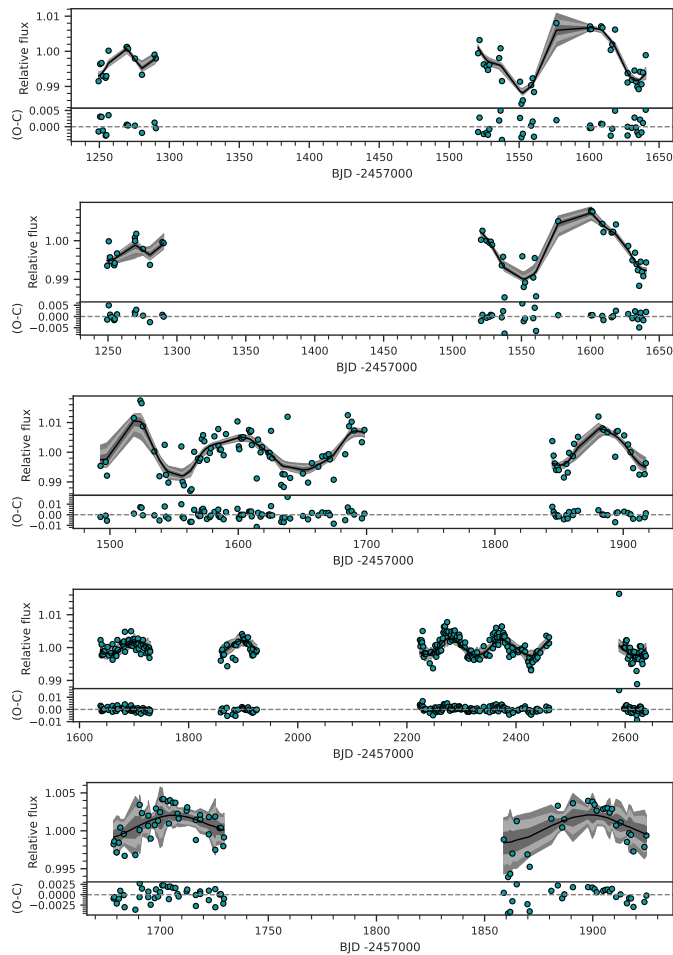


Fig. 3. Photometric time series of HNLib. The median models of the GP fit from 10 000 samples from the posterior are shown by the black lines and the grey shaded areas denote the 68 %, 95 %, and 99 % confidence intervals, respectively. *From top to bottom:* OSN-R, OSN-V, TJO, MEarth-tel14, and MEarth-tel15.

2014; Rajpaul et al. 2015). The parametrization in juliet for this kernel was described by Espinoza et al. (2019).

Because they are far away in time from the MEarth, OSN, and TJO observations and, thus, also from our RVs, we did not include the SuperWASP data in the fits, considering that the star could have been in a different stage of the activity cycle (Baliunas et al. 1995; Díez Alonso et al. 2019; Fuhrmeister et al. 2023). We used shared hyperparameters between the instruments for the rotation period and the parameters that describe the coherence and shape of the periodic components of the kernels (i.e., the quality factor and the difference in the quality factor of the dSHO kernel and the α and Γ parameters for the quasi-periodic kernel). The amplitude of the GP was considered individually for each instrument to account for potential wavelength dependencies and different states of activity. A summary of the GP hyperparameters and the used priors can be found in Table B.1. The MEarth data used comparison stars that are not M dwarfs (Irwin et al. 2011; Newton et al. 2016), introducing systematics. Their light curves were corrected by applying a simultaneous linear detrending of these data using the common mode parameter, which is based on the observations of all M-dwarf targets in the MEarth data combined to make a lower cadence (binned) comparison light curve (Newton et al. 2016, 2018).

Our fit with uninformative priors on the period between 10 d and 200 d resulted in a period of 94 ± 4 d using the QP-GP and 96 ± 2 d using the dSHO-GP. The photometry and the model from the dSHO-GP fit are shown in Fig. 3. The period from the photometric fit hence matches the ~ 94 d period of the spectroscopic activity indicators (see the left panels of Fig. 2), although it is the least significant of the two occurring aliases in most of the non-pre-whitened periodograms. One explanation for it could be that both ~ 125 d and ~ 94 d are close to harmonics of the long-term signals with periods of approximately one year, which we removed by pre-whitening the data. Since ~ 125 d matches a lower order harmonic, it is not unexpected that it is also more affected by residual signal in the data and thus increased in power in the GLS. In agreement with the $\log R'_{\text{HK}}$ measurements and the spectral activity indicators, we therefore established a rotation period of 96 ± 2 d for HNLib, the more precise value obtained from the dSHO-GP fit. In Table 3 we summarize the different values derived for the rotation period of the star using various methods (i.e., activity-rotation relationships, CARMENES spectroscopic activity indices, and photometric light curves) to ensure that all of them are consistent within their error bars. The error bars for the photometric cases come from our GP fit.

4.3. RV signal detection

We began the analysis of the RV data with a signal search using the GLS periodograms, as shown in Fig. 4. We considered a signal to be significant in the GLS periodogram if it has an FAP $< 1\%$. The CARMENES data (second row of Fig. 4) show two significant peaks at periods of ~ 36.1 d and ~ 113.1 d. When combining the CARMENES data with the HIRES and HARPS measurements (third row and following), both signals remain significant. However, multiple alias peaks appear on both sides of the 36-day signal due to the long time baseline and seasonal sampling of the combined data. Considering that this aliasing does not occur in the CARMENES data alone, we were consequently confident in the ~ 36.1 d period of the 36-day signal. Further, a signal with a FAP of almost 0.1% is visible near the period of the stellar rotation period (third row of Fig. 4), as determined in the previous section. The peak is distinct from the 113-day signal and not related by aliasing, as shown by the dashed lines in Fig. 4. Subtracting the 36-day signal with a sinusoidal model considerably increases the power of the 113-day signal in the residuals (fourth row of Fig. 4), but decreases the power of the signal at the rotation period. The residuals of a simultaneous sinusoidal fit of the 36-day signal and the 113-day period do not show any further significant signals (fifth row of Fig. 4). Since the period of ~ 113.1 d is close to the rotation period determined in Sect. 4.2, we assumed that it could be an imprint of the stellar activity onto the RVs and, consequently, performed a more in-depth analysis of this signal, which is presented in Sect. 4.5.

We verified that both significant RV signals are stable and coherent over the entire observational time baseline by producing the stacked Bayesian generalized Lomb-Scargle periodograms (s-BGLS, Mortier et al. 2015) shown in Fig. 5. The probability of the 36-day signal increases with time until a constant high degree is reached above one hundred observations. The aliases of 1 yr are also seen on both sides of the 36.1 d period, but with varying probability. With the increasing number of observations, the uncertainty of the period of the signal also becomes narrower, which is a behavior expected for signals with a Keplerian origin (Stock et al. 2020; Bluhm et al. 2021; Chaturvedi et al. 2022). Remarkably, the 113-day signal, for which we expected a more erratic behavior in case of a stellar activity origin, seems to be

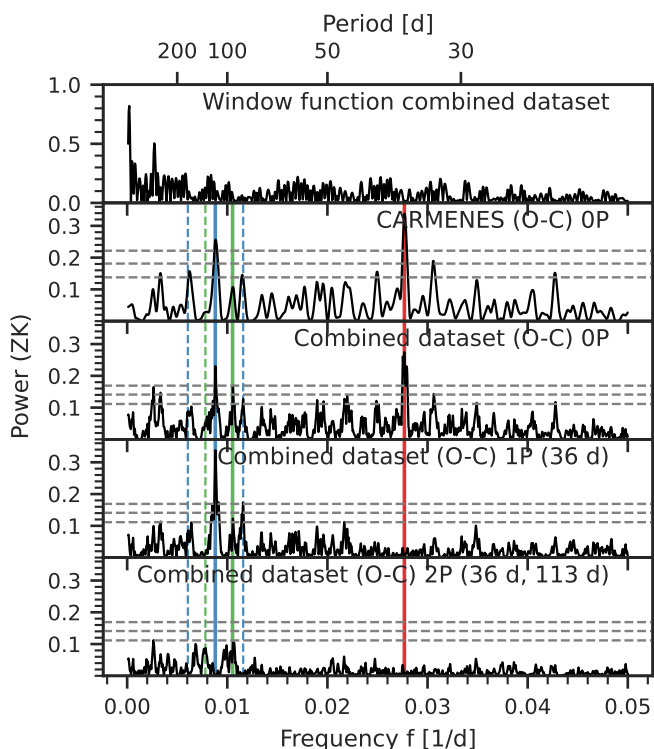


Fig. 4. Signal search with GLS periodograms in the RV data of HNLlib. The first panel shows the window function of the combined CARMENES, HIRES, and HARPS dataset. In the second panel, we show the GLS of only the CARMENES data. The subsequent panels present the GLS periodograms of the combined data. Each panel shows the residuals after subtracting models of increasing complexity. Inset texts describe the type of model that was applied to the data before the GLS was generated. A red solid line marks the period of the 36-day signal and the blue line shows the 113-day signal, while the green line denotes the rotation period of HNLlib. The 365 d alias frequencies of the 113-day signal and the stellar rotation period are highlighted by dashed lines. FAPs of 10, 1, and 0.1 % were calculated, using the analytical expression of Zechmeister & Kürster (2009) and are shown by the horizontal gray dashed lines.

also a stable signal after reaching ~ 80 observations. The region between 94 d and 96 d has an unstable behaviour revealed by changes in its width and probability when increasing the number of observations. As a result, it is likely to be the site of stellar activity.

4.4. RV modeling and planetary parameters

We found two potentially planetary signals in the periodogram analysis: an isolated signal with a period of 36.1 d and a second signal close to the stellar rotation with a period of 113.1 d. Following this, we conducted a model comparison based on the Bayesian evidence to find the model that explains the RV data the best. Our base assumption was that the RV data can be fully explained by stellar activity (= “0P-model”). For this model, we used GP modeling as in Sect. 4.2 to account for the quasi-periodic nature of such signals. To ensure consistency with the photometry, we applied the dSHO kernel in our analysis. Therefore, we used individual GP amplitudes for each instrument to consider the different scatter in the HIRES, HARPS, and CARMENES data. Furthermore, we made use of the determined stellar rotation period and adopted a normal prior centered on our

most precise measurement from the dSHO kernel of $P_{\text{rot}} \approx 96$ d, with three times the uncertainty of the photometric fit (± 6 d). We compared this activity-only model with two more complex models that assume the presence of further signals in the data. The first one additionally includes the 36-day signal using a Keplerian component with a uniform period prior between 30 d and 40 d (hereafter, the “1P-model”). We set t_0 , the time of inferior conjunction, between BJD = 2457433 and 2457450 to avoid a split posterior due to the aliasing. Further, we re-parametrized the eccentricity and the argument of periastron by $S_1 = \sqrt{e} \sin \omega$ and $S_2 = \sqrt{e} \cos \omega$ to allow for a uniform sampling between -1 and 1 (Eastman et al. 2013). In another fit, we additionally considered the 113-day signal by adding a second Keplerian component to the model. For this, we used a period prior between 100 d and 120 d and t_0 between BJD = 2457433 and 2457550 (hereafter, the “2P-model”). For both 1P and 2P models, we tested circular as well as eccentric models for the Keplerian signals. For all instruments, we set individual uninformed uniform priors for the RV offset and the jitter. A summary of the used priors can be found in Table B.2.

We found that the models including the 36-day signal are generally significantly (i.e., $\Delta \ln \mathcal{Z} > 5$; Trotta 2008) better than the model considering only the stellar activity (see Table 4). Likewise, the models including two Keplerian signals are mostly favored against the 1P-models, except for the model in which both planetary orbits are assumed to be eccentric. The highest evidence corresponds to the two planetary model, one eccentric orbit at 36 d and another circular orbit at 113 d, plus the dSHO kernel of P_{rot} at 96 d ($2P_{(36 \text{ d-ecc}, 113 \text{ d-circ})} + \text{dSHO-GP}_{(96 \text{ d})}$), which we chose as our final model for the further analysis (shown in Figs. 1 and 6). The inner planet orbits in a nearly circular orbit of eccentricity $0.079_{0.055}^{0.090}$. The posteriors from the fit for the planetary parameters and the GP can be found in Table 5 and Fig. A.1, and the instrumental posteriors in Table B.3. However, regardless of which model is chosen, all determined period and semi-amplitude combinations of the 36-day signal, which is the focus of our analysis, agree within their uncertainties (see Fig. A.2).

4.5. Investigation of the 113-day signal

Our findings about the 113-day signal up to this point can be summarized as follows: We found a signal in the RVs that is close to, but not exactly at, the period of the stellar rotation period, which we determined consistently from photometry and spectroscopic activity indicators. Furthermore, the stellar rotation period of 96 ± 2 d and the period in question at 113 d are not related by aliasing. In fact, we see evidence for a periodic signal in the RVs that coincides with the stellar rotation period that is distinct in period from the yearly aliases of the 113-day signal. Our analysis of the signal’s sBGLS periodogram and the model comparison show that it is very well described by a static Keplerian model.

4.6. Wavelength dependence

In the presence of strong stellar activity, we would expect a wavelength dependence of the RVs. A good first indicator for activity is the CRX, which expresses the RV-log λ -correlation (Zechmeister et al. 2018; Tal-Or et al. 2018; Jeffers et al. 2022). We used the CRX calculated from the CARMENES visual channel data to investigate the presence of stellar activity in HNLlib. However, the GLS periodogram of the CRX data does not show any peaks near the period in question (see Fig. A.3). Further,

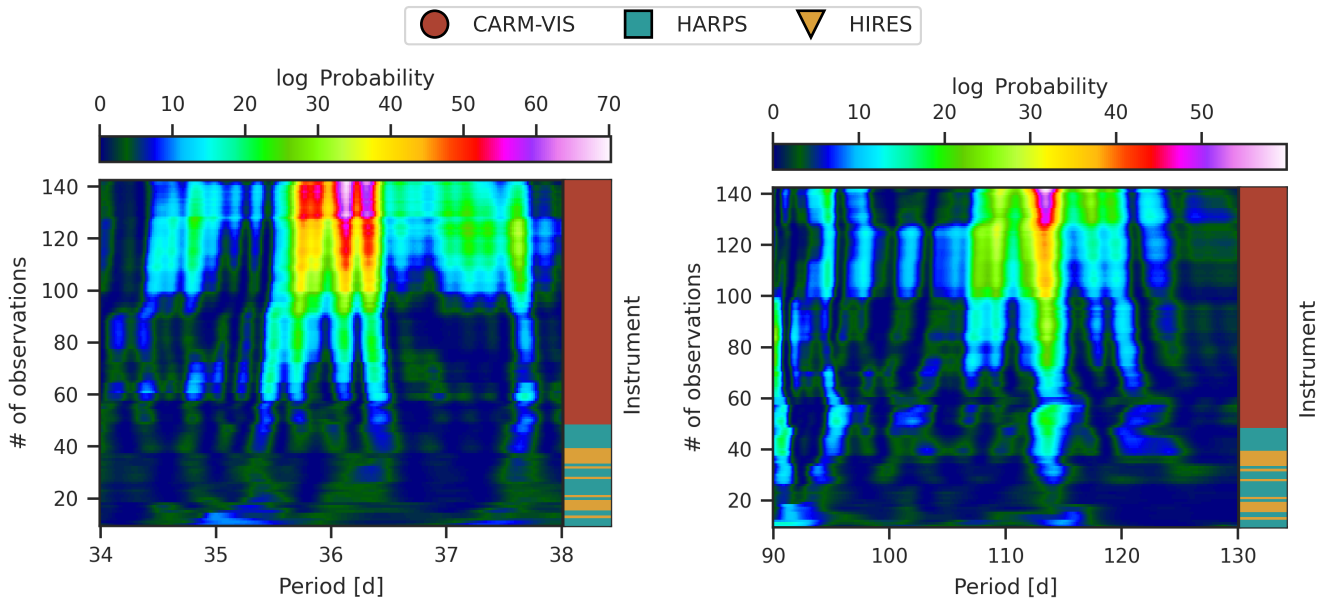


Fig. 5. Evolution of the s-BGLS periodogram of the CARMENES, HIRES, and HARPS RV data around 36 d (*left*) and in the region between 90 d and 130 d (*right*). The periodograms were generated using the residuals after subtracting the respective other periodicity, namely, the 113-d period in the left panel and the 36-d signal in the right panel. Both s-BGLS periodograms include the stellar rotation period. The colorbar on the top shows the Bayesian probability, where higher values are more likely. The right side of each plot indicates the instrument from which the individual added data points originate.

Table 4. Bayesian model comparison for the RV data.

Model	Priors [d]	Posteriors [d]	$\ln \mathcal{Z}$	$\Delta \ln \mathcal{Z}$	max. log likelihood
0P + dSHO _(96 d)	$\mathcal{N}_{\text{Prot,GP}}(96, 6)$	94.9273	-397.7	-15.0	-378.4
1P _(36 d-ecc) + dSHO _(96 d)	$\mathcal{U}_b(30, 40)$ $\mathcal{N}_{\text{Prot,GP}}(96, 6)$	36.1234 103.1397	-388.7	-6.0	-351.6
1P _(36 d-circ) + dSHO _(96 d)	$\mathcal{U}_b(30, 40)$ $\mathcal{N}_{\text{Prot,GP}}(96, 6)$	36.1185 101.1691	-388.6	-5.9	-355.4
2P _(36 d-ecc, 113 d-ecc) + dSHO _(96 d)	$\mathcal{U}_b(30, 40)$ $\mathcal{U}_c(100, 120)$ $\mathcal{N}_{\text{Prot,GP}}(96, 6)$	36.1154 113.4702 98.3681	-387.1	-4.4	-344.0
2P _(36 d-circ, 113 d-ecc) + dSHO _(96 d)	$\mathcal{U}_b(30, 40)$ $\mathcal{U}_c(100, 120)$ $\mathcal{N}_{\text{Prot,GP}}(96, 6)$	36.1234 113.4132 98.3081	-384.5	-1.8	-341.6
2P _(36 d-circ, 113 d-circ) + dSHO _(96 d)	$\mathcal{U}_b(30, 40)$ $\mathcal{U}_c(100, 120)$ $\mathcal{N}_{\text{Prot,GP}}(96, 6)$	36.1173 113.4677 99.2176	-382.9	-0.2	-344.1
2P_(36 d-ecc, 113 d-circ) + dSHO_(96 d)	$\mathcal{U}_b(30, 40)$ $\mathcal{U}_c(100, 120)$ $\mathcal{N}_{\text{Prot,GP}}(96, 6)$	36.1186 113.4634 97.6017	-382.7	0.0	-341.9

Notes. The model used for the final fit is the **2P_(36 d-ecc, 113 d-circ) + dSHO-GP_(96 d)** model highlighted in boldface. Wide, unconstrained priors are denoted as “blind.”

both in the original data and after removing the 36-day signal, there is no significant correlation between the RVs and the CRX.

Another method to investigate a potential wavelength dependence of a RV signal is to make use of the RVs computed for each échelle order (Bauer et al. 2020). To do this, we divided the CARMENES RVs into three roughly equal wavelength ranges and performed a fit to each of them to determine the semi-amplitude of the 113-day signal. For the fit, we took the results

from the best fit in Sect. 4.4 as normal priors for the 36-day signal and the dSHO-GP kernel, as well as the period of the 113-day signal. The prior of the semi-amplitude of the 113-day signal was set uniform between 0 m s^{-1} and 10 m s^{-1} . The results for the posterior distribution from those fits are depicted in Fig. 7. There are no significant discrepancies. The increase in amplitude and, at the same time, improvement in precision with increasing wavelength can be explained by the lower RV information con-

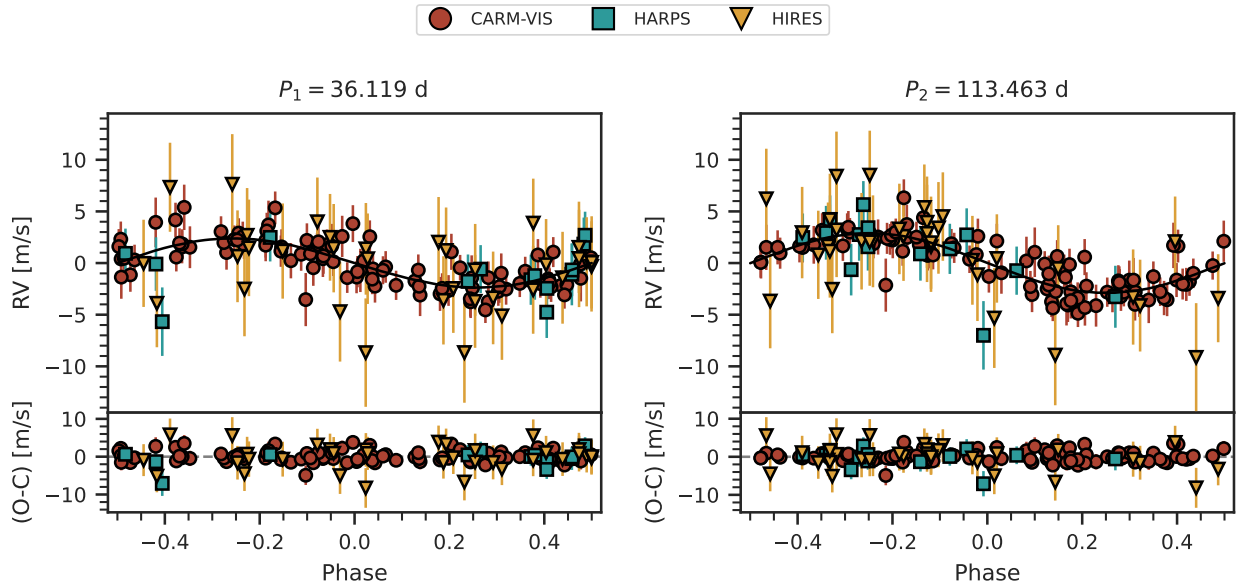


Fig. 6. Phased RV model for the HNLiB planets from the final $2P_{(36\text{d-ecc}, 113\text{d-circ})} + \text{dSHO-GP}_{(96\text{d})}$ model. The black lines show the median of 10 000 samples from the posterior. The residuals after subtracting the median models are shown in the lower panel.

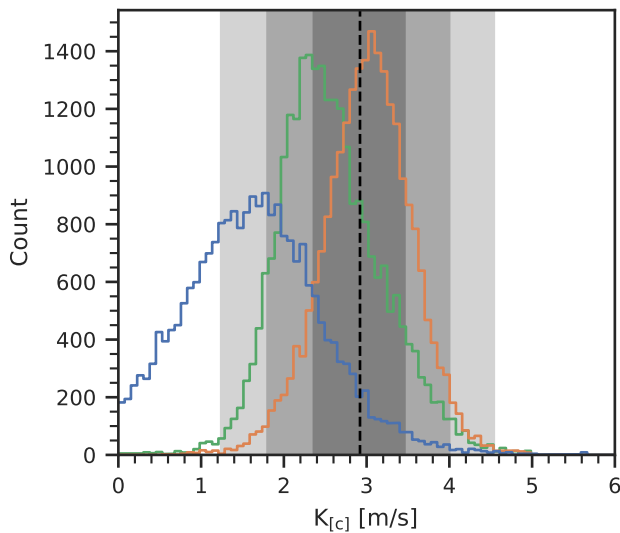


Fig. 7. RV semi-amplitudes of the 113-day signal (HNLiB[c]) as a function of wavelength for three different wavelength chunks of the whole CARMENES VIS wavelength domain. Blue: 5612–6491 Å, green: 6448–7613 Å, orange: 7576–9203 Å. The black dashed line indicates the best fit from Sect. 4.4, while the grey shades highlight the 1, 2, and 3 σ region around it.

tent in the bluer parts of the spectrum of the M4.0 V host star (e.g., [Reiners & Zechmeister 2020](#), and references therein).

5. Discussion

5.1. HNLiB b

The monitoring of the M dwarf HNLiB during our observing campaign within the CARMENES GTO program yielded a sub-Neptunian-mass planet discovery, namely HNLiB b. The minimum mass of the planet is $M_b \sin i = 5.46 \pm 0.75 M_\oplus$, and it orbits its host star in a nearly circular orbit at a separation

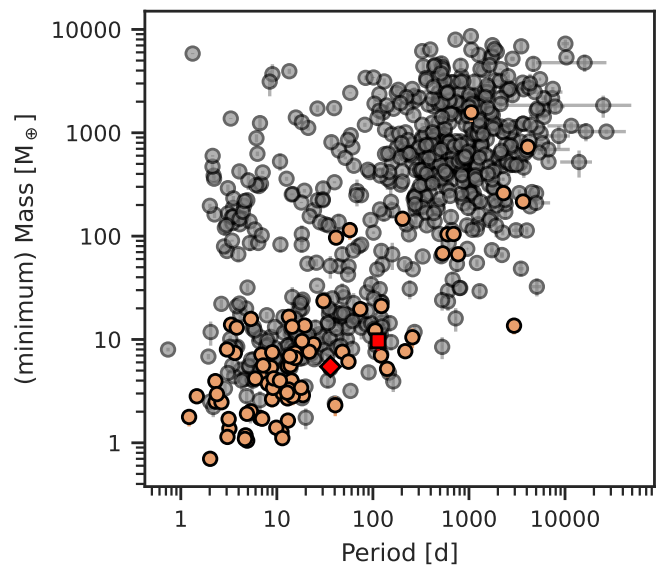


Fig. 8. Known exoplanets discovered with the RV method. Planets orbiting M dwarfs are marked with orange and the rest with grey circles. HNLiB b is highlighted by a red diamond and the planet candidate HNLiB [c] by a red square. For planets only detected by RVs, the minimum mass is depicted, while for planetary system with known inclination (e.g., from transits), the true mass is given. Based on the NASA Exoplanet Archive.

of $a_b = 0.1417 \pm 0.0023$ au with an orbital period of $P_b = 36.116 \pm 0.029$ d.

HNLiB b’s signal is unrelated to the stellar rotation period that we determined to be $P_{\text{rot}} = 96 \pm 2$ d and has no significant counterparts in the activity indicators. Furthermore, the stability and the coherence of the 36-d signal indicate a long-lived behavior, stable over the time span of our observations and thus providing strong arguments in favor of the planetary nature of HNLiB b. As it can be seen in Fig. 8, the planet adds to the sam-

Table 5. Posteriors of the planetary parameters and the GP component from the final model.

Parameter	Planet b	Planet [c]	Units
<i>Planetary posteriors</i>			
P	$36.116^{+0.027}_{-0.029}$	$113.46^{+0.19}_{-0.20}$	d
t_0	$2\,457\,436.3^{+1.4}_{-1.4}$	$2\,457\,492.8^{+3.6}_{-3.3}$	d
$\sqrt{e} \cos \omega$	$0.03^{+0.22}_{-0.23}$
$\sqrt{e} \sin \omega$	$-0.11^{+0.23}_{-0.21}$
K	$2.59^{+0.34}_{-0.34}$	$2.92^{+0.54}_{-0.56}$	m s^{-1}
<i>Derived planetary parameters</i>			
$M \sin i$	$5.46^{+0.75}_{-0.75}$	$9.7^{+1.9}_{-1.9}$	M_{\oplus}
e	$0.079^{+0.090}_{-0.055}$
a	$0.1417^{+0.0023}_{-0.0023}$	$0.3040^{+0.0048}_{-0.0051}$	au
S	$0.503^{+0.018}_{-0.016}$	$0.1094^{+0.0039}_{-0.0035}$	S_{\oplus}
$T_{\text{eq}}(1-A)^{-1/4}$	$234.4^{+5.5}_{-5.3}$	$160.1^{+3.7}_{-3.7}$	K
<i>GP posteriors</i>			
$\sigma_{\text{GP, CARMENES}}$	$3.47^{+1.04}_{-0.67}$		m s^{-1}
$\sigma_{\text{GP, HIRES}}$	$6.88^{+1.73}_{-2.00}$		m s^{-1}
$\sigma_{\text{GP, HARPS}}$	$2.35^{+1.51}_{-1.03}$		m s^{-1}
f_{GP}	$0.33^{+0.38}_{-0.25}$...
$Q_{0,\text{GP}}$	$0.22^{+0.37}_{-0.10}$...
dQ_{GP}	$122.00^{+23\,938}_{-114}$...
$P_{\text{rot, GP}}$	96 ± 2		d

Notes. Error bars denote the 68% posterior confidence intervals.

ple of small, sub-Neptunian mass planets, which make up the bulk of planets detected to orbit M dwarfs on short orbits and that are predicted to be the most abundant planet type around M dwarfs (Dressing & Charbonneau 2015; Sabotta et al. 2021; Pinamonti et al. 2022).

Kopparapu et al. (2013, 2014) calculated conservative estimations of the inner HZ around stars with stellar effective temperatures in the range 2600–7200 K for planetary masses between 0.1 and $5 M_{\oplus}$. Taking into account the runaway greenhouse effect for $5 M_{\oplus}$ planets such as HN Lib b, the inner edge of HN Lib’s HZ is accordingly placed at 0.101 au. With an instellation of $S \approx 0.50 S_{\oplus}$ and a semi-major axis of 0.142 au, HN Lib b thus resides in the conservative HZ of HN Lib. At a distance of only 6.25 pc, HN Lib is one of the closest systems to Earth with a planet in the conservative HZ.

In the two extreme cases of the Bond albedo, $A = 0.0$ and $A = 0.65$, the T_{eq} for HN Lib b falls in the range of 243–174 K for a non-reflecting planet and for a highly reflecting planet, respectively. In Fig. 9 we compare the position of HN Lib b with other known habitable zone sub-Neptune-type and super-Earth planets with (minimum) mass measurements around M dwarfs. However, as for all planets in this regime, the actual habitability depends on many factors. The most decisive is probably the nature of its atmosphere (Kaltenegger 2017).

Unfortunately, HN Lib has not been observed by NASA’s Transiting Exoplanet Survey Satellite (*TESS*), nor are any such

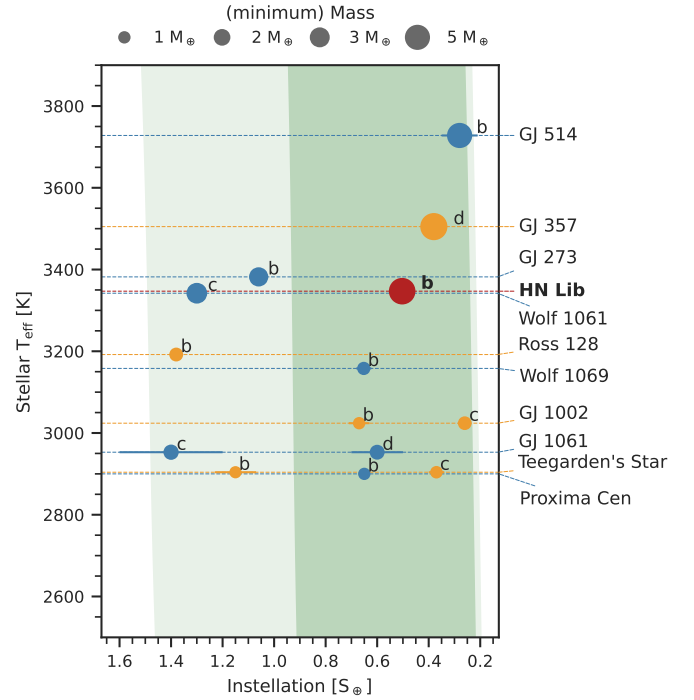


Fig. 9. Comparison to other small (i.e., $M \sin i \leq 10 M_{\oplus}$) potentially habitable planets orbiting M-dwarf stars at less than 10 pc from the Sun. HN Lib b is highlighted in red, while the other planets are iterated between orange and blue for better distinguishability. The light green and dark green shaded areas denote the optimistic and conservative HZs of Kopparapu et al. (2013, 2014), respectively. The planet list was taken from the habitable planets catalog of the Planetary Habitability Laboratory at the University of Puerto Rico and merged with the composite planetary parameters table of the NASA Exoplanet Archive.

observations planned for future *TESS* sectors. Given the ambiguity of the mass-radius relation for small planets (e.g., Fulton et al. 2017; Van Eylen et al. 2018; Petigura 2020; Cloutier & Menou 2020), we thus only can hypothesize about its size and composition. Following the recent empirical analysis of small, transiting planets with mass measurements by Luque & Pallé (2022), there are three different plausible compositions given the mass of HN Lib b: a rocky planet with an Earth-like density, a water-rich planet, and a gaseous planet with an extended hydrogen atmosphere. Applying the theoretical mass-radius relationships by Zeng et al. (2019) to the different possibilities results in radii of $\sim 1.6 R_{\oplus}$ for an Earth-like planet, $\sim 2.0 R_{\oplus}$ for a water-rich planet, and $\sim 2.4 R_{\oplus}$ for 1% of hydrogen added to an Earth-like core (assuming an equilibrium temperature of 300 K in all three cases). The resulting Earth similarity index (Schulze-Makuch et al. 2011) for a rocky planet would be 0.60, comparable to TRAPPIST-1 g (Gillon et al. 2017; Grimm et al. 2018; Ducrot et al. 2020; Agol et al. 2021) or the recently discovered GJ 1002 b (Suárez Mascareño et al. 2023). For a full transit, the depth would be in the range of ~ 1600 – 5400 ppm taking into account the different possible compositions. However, the probability that our planet transits is low ($0.98^{+1.02}_{-0.94}\%$).

We explored the high energy environment of HN Lib b to test for the habitability conditions on the planet. There are no positive X-ray detections of HN Lib in the literature (Wood et al. 1994; Schmitt et al. 1995), but Stelzer et al. (2013) calculated an upper limit of $\log L_X < 26.80$. As an alternative approach, we used the rotation period of 96 ± 2 d to calculate the expected

X-ray emission, based on the relations of [Wright et al. \(2011\)](#), resulting in $\log L_X \sim 26.9$, in approximate agreement with the aforementioned upper limit. We then used the relationships in [Sanz-Forcada et al. \(2011\)](#) to calculate the extreme ultraviolet (EUV) luminosity (L_{EUV}) corresponding to this X-ray flux, $\log L_{\text{EUV}} = 27.9$, and the expected (upper limit) mass loss rate in an energy-limited approach, $1.8 \times 10^9 \text{ g s}^{-1}$ or $0.0097 M_{\oplus} \text{ Gyr}^{-1}$. This mass loss rate is too low to pose any problem for the present stability of the planet’s atmosphere, which is consistent with the planet’s location in the potentially HZ of HNLib. The stellar age based on the X-ray luminosity is quite uncertain (~ 7 Gyr, [Sanz-Forcada et al. 2011](#)), but it is not consistent with values as low as 0.8 Gyr, which would otherwise imply X-ray activity approaching saturation, $\log L_X \sim 28.4$, and a shorter rotation period.

5.2. HN Lib [c]

The RV observations show another significant signal at a period of ~ 113 d, close to the stellar rotation period of 96 ± 2 d. Our model comparison shows that the signal is reasonably well described by a circular Keplerian orbit and, following the sBGLS analysis, seems to be reasonably stable over the whole period of our observations, spanning 21 years. When analyzing its wavelength dependency, we found no significant changes in the amplitude of the signal that would hint at its origins coming from stellar activity. However, given the proximity to the stellar rotation period, we could not fully rule out this scenario (especially due to the presence of differential rotation) and thus report it as a planet candidate. HN Lib [c] has a minimum mass of $9.7 \pm 1.9 M_{\oplus}$ and orbits HN Lib at a separation of 0.3040 ± 0.0051 au. In contrast to HN Lib b, the orbit lies outside the HZ of HN Lib. As for planet b, predictions about its composition are ambiguous because it resides in the same mass regime. However, due to the orbit beyond the ice line of HNLib, an ice-rich planet is very likely ([Burn et al. 2021](#)). In combination with the also comparatively massive inner companion, the planetary system of HN Lib is therefore very interesting with regard to the formation and evolution of systems with planets in the HZ.

6. Summary

The newly discovered planet HN Lib b orbits a nearby M4.0 V star and has a minimum mass of $M_b \sin i = 5.46 \pm 0.75 M_{\oplus}$. Given the ambiguity of the radius in this mass range, this planet could be either rocky, a water-rich, or gaseous. The orbital period of the planet, $P_b = 36.116 \pm 0.029$ d, corresponds to a separation to its host of $a_b = 0.1417 \pm 0.0023$ au centered in the conservative HZ of HN Lib ($S \approx 0.50 S_{\oplus}$). HN Lib b is one of the closest planets orbiting its host in the HZ as seen from Earth and, assuming that it has a rocky composition, its Earth similarity index would be 0.60.

Additionally, our RV measurements show another significant signal with a period of $P_{[c]} = 113.46 \pm 0.20$ d, which is close to the stellar rotation period of $P_{\text{rot}} = 96 \pm 2$ d that we determined from photometric measurements – and which was additionally validated with spectroscopic activity indicators. Since we can neither confirm nor exclude that the signal is an imprint of stellar activity, although we do know is stable over the time span of our observations, we report it to be a planet candidate with a minimum mass of $9.7 \pm 1.9 M_{\oplus}$.

Acknowledgements. We wish to thank the anonymous referee for helpful comments and suggestions, which helped to improve the manuscript. CARMENES is an instrument at the Centro Astronómico Hispano en Andalucía (CAHA) at Calar

Alto (Almería, Spain), operated jointly by the Junta de Andalucía and the Instituto de Astrofísica de Andalucía (CSIC). CARMENES was funded by the German Max-Planck-Gesellschaft (MPG), the Spanish Consejo Superior de Investigaciones Científicas (CSIC), the European Union through FEDER/ERF funds, and the members of the CARMENES Consortium (Max-Planck-Institut für Astronomie, Instituto de Astrofísica de Andalucía, Landessternwarte Königstuhl, Institut de Ciències de l’Espai, Institut für Astrophysik Göttingen, Universidad Complutense de Madrid, Thüringer Landessternwarte Tautenburg, Instituto de Astrofísica de Canarias, Hamburger Sternwarte, Centro de Astrobiología and Centro Astronómico Hispano-Alemán), with additional contributions by the Spanish Ministry of Economy, the state of Baden-Württemberg and Niedersachsen, the Klaus Tschira Foundation (KTS), the Deutsche Forschungsgemeinschaft (DFG) via the Research Unit FOR2544 “Blue Planets around Red Stars”, and by the Junta de Andalucía. This work was based on data from the CARMENES data archive at CAB (CSIC-INTA). Data were partly collected with the 90 cm telescope at the Sierra Nevada Observatory (OSN) operated by the Instituto de Astrofísica de Andalucía (IAA-CSIC). We acknowledge the telescope operators from Observatori Astronòmic del Montsec, Sierra Nevada Observatory, and CAHA. We acknowledge financial support from the Agencia Estatal de Investigación 10.13039/501100011033 of the Ministerio de Ciencia e Innovación and the ERDF “A way of making Europe” through projects PID2019-109522GB-C5[1,2,3,4] PGC2018-098153-B-C3[1,3] and the Centre of Excellence “Severo Ochoa” and “María de Maeztu” awards to the Instituto de Astrofísica de Canarias (CEX2019-000920-S), Instituto de Astrofísica de Andalucía (SEV-2017-0709), and Centro de Astrobiología (MDM-2017-0737), the Generalitat de Catalunya/CERCA programme, and the Israel Science Foundation (grant No. 1404/22). This research has made use of the NASA Exoplanet Archive, which is operated by the California Institute of Technology, under contract with the National Aeronautics and Space Administration under the Exoplanet Exploration Program.

References

- Agol, E., Dorn, C., Grimm, S. L., et al. 2021, *PSJ*, 2, 1
- Allard, F., Homeier, D., Freytag, B., & Sharp, C. M. 2012, in *EAS Publications Series*, ed. C. Reylé, C. Charbonnel, & M. Schultheis, Vol. 57, 3–43
- Alonso-Floriano, F. J., Morales, J. C., Caballero, J. A., et al. 2015, *A&A*, 577, A128
- Ambikasaran, S., Foreman-Mackey, D., Greengard, L., Hogg, D. W., & O’Neil, M. 2015, *IEEE Transactions on Pattern Analysis and Machine Intelligence*, 38, 252
- Astudillo-Defru, N., Delfosse, X., Bonfils, X., et al. 2017, *A&A*, 600, A13
- Baliunas, S. L., Donahue, R. A., Soon, W. H., et al. 1995, *ApJ*, 438, 269
- Baraffe, I., Homeier, D., Allard, F., & Chabrier, G. 2015, *A&A*, 577, A42
- Bauer, F. F., Zechmeister, M., Kaminski, A., et al. 2020, *A&A*, 640, A50
- Bluhm, P., Pallé, E., Molaverdikhani, K., et al. 2021, *A&A*, 650, A78
- Bonfils, X., Delfosse, X., Udry, S., et al. 2013, *A&A*, 549, A109
- Burn, R., Schlecker, M., Mordasini, C., et al. 2021, *A&A*, 656, A72
- Caballero, J. A., Cortés-Contreras, M., Alonso-Floriano, F. J., et al. 2016a, in *19th Cambridge Workshop on Cool Stars, Stellar Systems, and the Sun (CS19)*, 148
- Caballero, J. A., González-Álvarez, E., Brady, M., et al. 2022, *A&A*, 665, A120
- Caballero, J. A., Guàrdia, J., López del Fresno, M., et al. 2016b, in *Society of Photo-Optical Instrumentation Engineers (SPIE) Conference Series*, Vol. 9910, *Observatory Operations: Strategies, Processes, and Systems VI*, ed. A. B. Peck, R. L. Seaman, & C. R. Benn, 99100E
- Chaturvedi, P., Bluhm, P., Nagel, E., et al. 2022, *A&A*, 666, A155
- Cifuentes, C., Caballero, J. A., Cortés-Contreras, M., et al. 2020, *A&A*, 642, A115
- Cloutier, R. & Menou, K. 2020, *AJ*, 159, 211
- Collins, K. A., Kielkopf, J. F., Stassun, K. G., & Hessman, F. V. 2017, *AJ*, 153, 77
- Colomé, J., Casteels, K., Ribas, I., & Francisco, X. 2010, in *Society of Photo-Optical Instrumentation Engineers (SPIE) Conference Series*, Vol. 7740, *Software and Cyberinfrastructure for Astronomy*, ed. N. M. Radziwill & A. Bridger, 77403K
- Colome, J. & Ribas, I. 2006, *IAU Special Session*, 6, 11
- Cortés-Contreras, M., Béjar, V. J. S., Caballero, J. A., et al. 2017, *A&A*, 597, A47
- David, T. J., Petigura, E. A., Luger, R., et al. 2019, *ApJ*, 885, L12
- Davison, C. L., White, R. J., Henry, T. J., et al. 2015, *AJ*, 149, 106
- Dieterich, S. B., Henry, T. J., Golimowski, D. A., Krist, J. E., & Tanner, A. M. 2012, *AJ*, 144, 64
- Díez Alonso, E., Caballero, J. A., Montes, D., et al. 2019, *A&A*, 621, A126
- Dressing, C. D. & Charbonneau, D. 2013, *ApJ*, 767, 95
- Dressing, C. D. & Charbonneau, D. 2015, *ApJ*, 807, 45
- Ducrot, E., Gillon, M., Delrez, L., et al. 2020, *A&A*, 640, A112

- Eastman, J., Gaudi, B. S., & Agol, E. 2013, *PASP*, 125, 83
- Espinoza, N., Kossakowski, D., & Brahm, R. 2019, *MNRAS*, 490, 2262
- Foreman-Mackey, D., Agol, E., Ambikasaran, S., & Angus, R. 2017, *AJ*, 154, 220
- Fuhrmeister, B., Czesla, S., Hildebrandt, L., et al. 2020, *A&A*, 640, A52
- Fuhrmeister, B., Czesla, S., Perdelwitz, V., et al. 2023, *A&A*, 670, A71
- Fulton, B. J., Petigura, E. A., Blunt, S., & Sinukoff, E. 2018, *PASP*, 130, 044504
- Fulton, B. J., Petigura, E. A., Howard, A. W., et al. 2017, *AJ*, 154, 109
- Gaia Collaboration, Brown, A. G. A., Vallenari, A., et al. 2021, *A&A*, 649, A1
- Gaia Collaboration, Vallenari, A., Brown, A. G. A., et al. 2022, arXiv e-prints, arXiv:2208.00211
- Gaidos, E., Mann, A. W., Lepine, S., et al. 2015, *VizieR Online Data Catalog*, J/MNRAS/443/2561
- Gillen, E., Briegal, J. T., Hodgkin, S. T., et al. 2020, *MNRAS*, 492, 1008
- Gillon, M., Triaud, A. H. M. J., Demory, B.-O., et al. 2017, *Nature*, 542, 456
- Gliese, W. 1969, *Veröffentlichungen des Astronomischen Rechen-Instituts Heidelberg*, 22, 1
- Grimm, S. L., Demory, B.-O., Gillon, M., et al. 2018, *A&A*, 613, A68
- Hawley, S. L., Gizis, J. E., & Reid, I. N. 1996, *AJ*, 112, 2799
- Haywood, R. D., Collier Cameron, A., Queloz, D., et al. 2014, *MNRAS*, 443, 2517
- Hinz, J. L., McCarthy, Donald W., J., Simons, D. A., et al. 2002, *AJ*, 123, 2027
- Hippke, M., David, T. J., Mulders, G. D., & Heller, R. 2019, *AJ*, 158, 143
- Hosey, A. D., Henry, T. J., Jao, W.-C., et al. 2015, *AJ*, 150, 6
- Ida, S. & Lin, D. N. C. 2005, *ApJ*, 626, 1045
- Irwin, J., Berta, Z. K., Burke, C. J., et al. 2011, *ApJ*, 727, 56
- Irwin, J. M., Berta-Thompson, Z. K., Charbonneau, D., et al. 2015, in *18th Cambridge Workshop on Cool Stars, Stellar Systems, and the Sun*, Vol. 18, 767–772
- Jackson, J. & Turner, J. B. G. 1952, *MNRAS*, 112, 94
- Jameson, R. F., Sherrington, M. R., & Giles, A. B. 1983, *MNRAS*, 205, 39P
- Jeffers, S. V., Barnes, J. R., Schöfer, P., et al. 2022, *A&A*, 663, A27
- Jódar, E., Pérez-Garrido, A., Díaz-Sánchez, A., et al. 2013, *MNRAS*, 429, 859
- Johnson, D. R. H. & Soderblom, D. R. 1987, *AJ*, 93, 864
- Kaltenegger, L. 2017, *ARA&A*, 55, 433
- Kasting, J. F., Whitmire, D. P., & Reynolds, R. T. 1993, *Icarus*, 101, 108
- Kipping, D. M., Hartman, J., Buchhave, L. A., et al. 2013, *ApJ*, 770, 101
- Kochanek, C. S., Shappee, B. J., Stanek, K. Z., et al. 2017, *PASP*, 129, 104502
- Kopparapu, R. K., Ramirez, R., Kasting, J. F., et al. 2013, *ApJ*, 765, 131
- Kopparapu, R. K., Ramirez, R. M., Schottelkotte, J., et al. 2014, *ApJ*, 787, L29
- Kossakowski, D., Kemmer, J., Bluhm, P., et al. 2021, *A&A*, 656, A124
- Kossakowski, D., Kürster, M., Trifonov, T., et al. 2023, *A&A*, 670, A84
- Kukarkin, B. V. & Kholopov, P. N. 1982, *New catalogue of suspected variable stars*
- Leggett, S. K. 1992, *ApJS*, 82, 351
- Luque, R. & Pallé, E. 2022, *Science*, 377, 1211
- Maldonado, J., Micela, G., Baratella, M., et al. 2020, *A&A*, 644, A68
- Mann, A. W., Feiden, G. A., Gaidos, E., Boyajian, T., & von Braun, K. 2015, *ApJ*, 804, 64
- Marfil, E., Taberero, H. M., Montes, D., et al. 2021, *A&A*, 656, A162
- Mayor, M., Pepe, F., Queloz, D., et al. 2003, *The Messenger*, 114, 20
- Mortier, A., Faria, J. P., Correia, C. M., Santerne, A., & Santos, N. C. 2015, *A&A*, 573, A101
- Nakajima, T., Durrance, S. T., Golimowski, D. A., & Kulkarni, S. R. 1994, *ApJ*, 428, 797
- Newton, E. R., Irwin, J., Charbonneau, D., et al. 2016, *ApJ*, 821, 93
- Newton, E. R., Mondrik, N., Irwin, J., Winters, J. G., & Charbonneau, D. 2018, *AJ*, 156, 217
- Oppenheimer, B. R., Golimowski, D. A., Kulkarni, S. R., et al. 2001, *AJ*, 121, 2189
- Passegger, V. M., Reiners, A., Jeffers, S. V., et al. 2018, *A&A*, 615, A6
- Perdelwitz, V., Mittag, M., Tal-Or, L., et al. 2021, *A&A*, 652, A116
- Petigura, E. A. 2020, *AJ*, 160, 89
- Pinamonti, M., Sozzetti, A., Maldonado, J., et al. 2022, *A&A*, 664, A65
- Plez, B. 2012, *Turbospectrum: Code for spectral synthesis*, *Astrophysics Source Code Library*, record ascl:1205.004
- Pojmanski, G. 1997, *Acta Astron.*, 47, 467
- Pollacco, D. L., Skillen, I., Collier Cameron, A., et al. 2006, *PASP*, 118, 1407
- Quirrenbach, A., Amado, P. J., Caballero, J. A., et al. 2014, in *Society of Photo-Optical Instrumentation Engineers (SPIE) Conference Series*, Vol. 9147, *Ground-based and Airborne Instrumentation for Astronomy V*, ed. S. K. Ramsay, I. S. McLean, & H. Takami, 91471F
- Rajpaul, V., Aigrain, S., Osborne, M. A., Reece, S., & Roberts, S. 2015, *MNRAS*, 452, 2269
- Rajpurohit, A. S., Allard, F., Rajpurohit, S., et al. 2018, *A&A*, 620, A180
- Raymond, S. N., Scalzo, J., & Meadows, V. S. 2007, *ApJ*, 669, 606
- Reiners, A., Shulyak, D., Käpylä, P. J., et al. 2022, *A&A*, 662, A41
- Reiners, A. & Zechmeister, M. 2020, *ApJS*, 247, 11
- Reiners, A., Zechmeister, M., Caballero, J. A., et al. 2018, *A&A*, 612, A49
- Ribas, I., Reiners, A., Zechmeister, M., et al. 2023, arXiv e-prints, arXiv:2302.10528
- Rodenbeck, K., Heller, R., Hippke, M., & Gizon, L. 2018, *A&A*, 617, A49
- Rodríguez, E., García, J. M., Costa, V., et al. 2010, *MNRAS*, 408, 2149
- Rojas-Ayala, B., Covey, K. R., Muirhead, P. S., & Lloyd, J. P. 2012, *ApJ*, 748, 93
- Sabotta, S., Schlecker, M., Chaturvedi, P., et al. 2021, *A&A*, 653, A114
- Sanz-Forcada, J., Micela, G., Ribas, I., et al. 2011, *A&A*, 532, A6
- Schlecker, M., Burn, R., Sabotta, S., et al. 2022, *A&A*, 664, A180
- Schmitt, J. H. M. M., Fleming, T. A., & Giampapa, M. S. 1995, *ApJ*, 450, 392
- Schöfer, P., Jeffers, S. V., Reiners, A., et al. 2019, *A&A*, 623, A44
- Schönfeld, E. 1886, *Eds Marcus and Weber's Verlag*, 0
- Schulze-Makuch, D., Méndez, A., Fairén, A. G., et al. 2011, *Astrobiology*, 11, 1041
- Schweitzer, A., Passegger, V. M., Cifuentes, C., et al. 2019, *A&A*, 625, A68
- Shappee, B. J., Prieto, J. L., Grupe, D., et al. 2014, *ApJ*, 788, 48
- Simons, D. A., Henry, T. J., & Kirkpatrick, J. D. 1996, *AJ*, 112, 2238
- Skrutskie, M. F., Cutri, R. M., Stiening, R., et al. 2006, *AJ*, 131, 1163
- Skrutskie, M. F., Forrest, W. J., & Shure, M. 1989, *AJ*, 98, 1409
- Soubiran, C., Jasniewicz, G., Chemin, L., et al. 2018, *A&A*, 616, A7
- Speagle, J. S. 2020, *MNRAS*, 493, 3132
- Stelzer, B., Marino, A., Micela, G., López-Santiago, J., & Liefke, C. 2013, *MNRAS*, 431, 2063
- Stock, S., Nagel, E., Kemmer, J., et al. 2020, *A&A*, 643, A112
- Suárez Mascareño, A., González-Álvarez, E., Zapatero Osorio, M. R., et al. 2023, *A&A*, 670, A5
- Taberero, H. M., Marfil, E., Montes, D., & González Hernández, J. I. 2022, *A&A*, 657, A66
- Tal-Or, L., Trifonov, T., Zucker, S., Mazeh, T., & Zechmeister, M. 2019, *MNRAS*, 484, L8
- Tal-Or, L., Zechmeister, M., Reiners, A., et al. 2018, *A&A*, 614, A122
- Tanner, A. M., Gelino, C. R., & Law, N. M. 2010, *PASP*, 122, 1195
- Tarter, J. C., Backus, P. R., Mancinelli, R. L., et al. 2007, *Astrobiology*, 7, 30
- Trifonov, T. 2019, *The Exo-Striker: Transit and radial velocity interactive fitting tool for orbital analysis and N-body simulations*, *Astrophysics Source Code Library*, record ascl:1906.004
- Trifonov, T., Tal-Or, L., Zechmeister, M., et al. 2020, *A&A*, 636, A74
- Trotta, R. 2008, *Contemporary Physics*, 49, 71
- Tuomi, M., Jones, H. R. A., Barnes, J. R., Anglada-Escudé, G., & Jenkins, J. S. 2014, *MNRAS*, 441, 1545
- Udry, S., Bonfils, X., Delfosse, X., et al. 2007, *A&A*, 469, L43
- Van Eylen, V., Agentoft, C., Lundkvist, M. S., et al. 2018, *MNRAS*, 479, 4786
- Vogt, S. S., Allen, S. L., Bigelow, B. C., et al. 1994, in *Society of Photo-Optical Instrumentation Engineers (SPIE) Conference Series*, Vol. 2198, *Instrumentation in Astronomy VIII*, ed. D. L. Crawford & E. R. Craine, 362
- Ward-Duong, K., Patience, J., De Rosa, R. J., et al. 2015, *MNRAS*, 449, 2618
- Weis, E. W. 1994, *AJ*, 107, 1135
- Wolf, M. 1925, *Astronomische Nachrichten*, 225, 215
- Wood, B. E., Brown, A., Linsky, J. L., et al. 1994, *ApJS*, 93, 287
- Wright, N. J., Drake, J. J., Mamajek, E. E., & Henry, G. W. 2011, *ApJ*, 743, 48
- Zechmeister, M. & Kürster, M. 2009, *A&A*, 496, 577
- Zechmeister, M., Kürster, M., & Endl, M. 2009, *A&A*, 505, 859
- Zechmeister, M., Reiners, A., Amado, P. J., et al. 2018, *A&A*, 609, A12
- Zeng, L., Jacobsen, S. B., Sasselov, D. D., et al. 2019, *Proceedings of the National Academy of Science*, 116, 9723

Appendix A: Additional figures

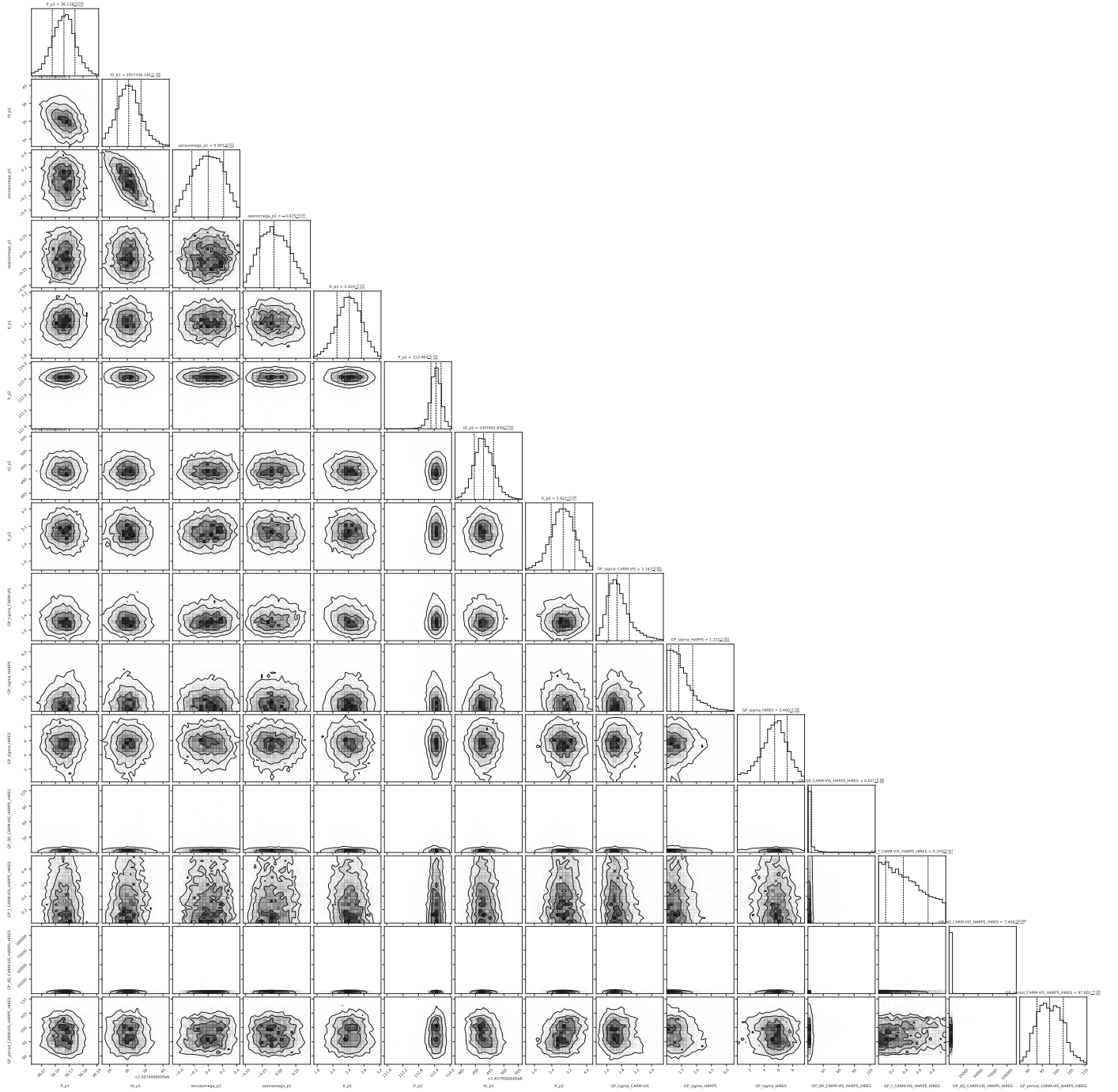


Fig. A.1. Posterior distributions of the fitted planetary and GP parameters of the HNLiB system as obtained from the final $IP_{(36\text{ d-ecc})} + \text{dSHO-GP}_{(113\text{ d})}$ fit. The vertical dashed lines indicate the 16, 50, and 84% quantiles that were used to define the optimal values and their associated 1σ uncertainty.

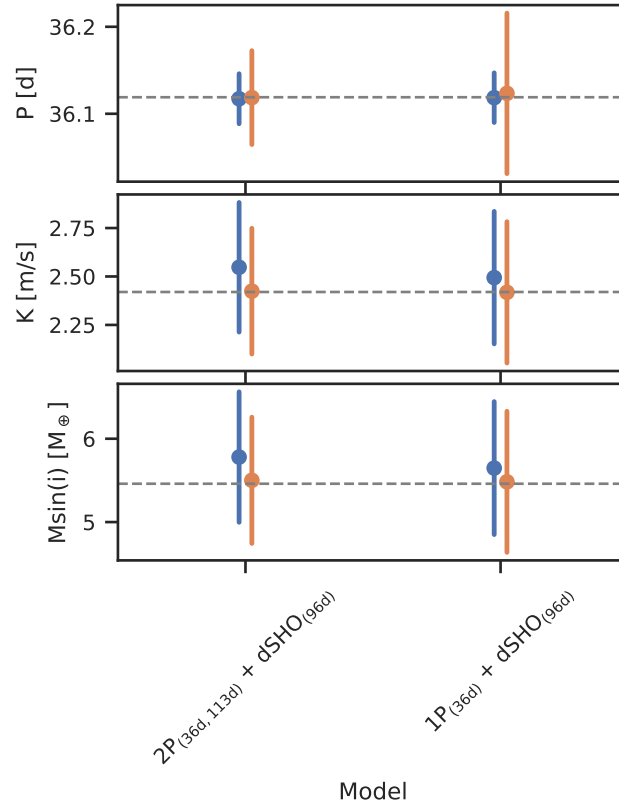


Fig. A.2. Posterior distributions of the period, semi-amplitude, and determined mass of the 36-day planet for the different models. The blue markers depict the circular models and the orange markers the eccentric models.

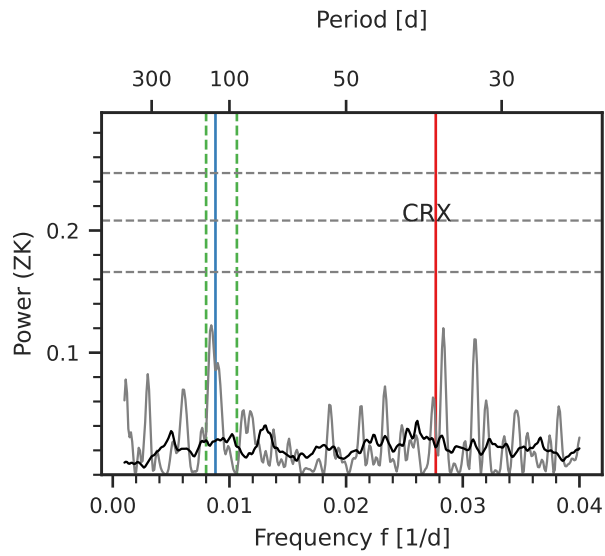


Fig. A.3. GLS periodogram of the CRX activity indicator.

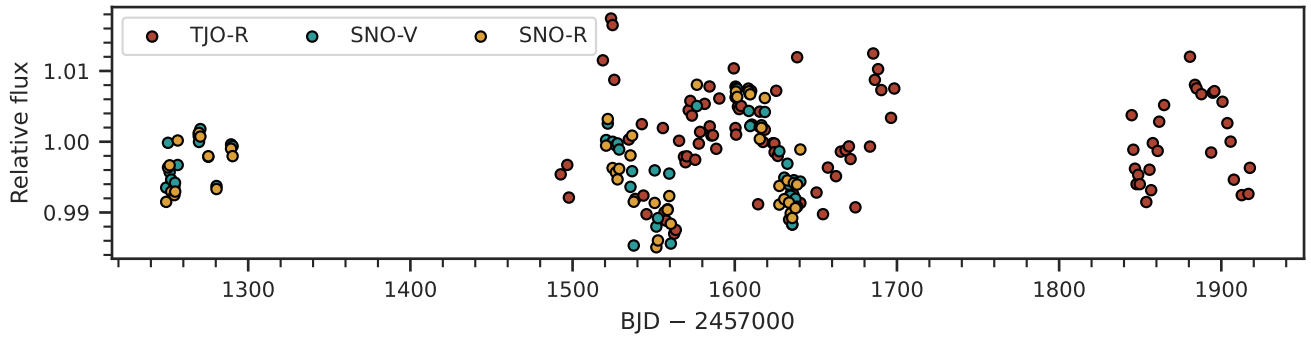


Fig. A.4. Comparison of the TJO and OSN photometry after the CAFM detrending.

Appendix B: Tables**Table B.1.** Priors used to determine the photometric rotation period of HNLib.

Parameter	Prior	Unit	Description
<i>dSHO-GP parameters</i>			
σ_{GP}	$\mathcal{J}(1, 10^6)$	ppm	Standard deviation of the GP, individual for each instrument but shared between the MEarth telescopes
f_{GP}	$\mathcal{U}(0.0, 1.0)$...	Fractional amplitude of the secondary mode compared to the primary mode, shared between all instruments
$Q_{0,\text{GP}}$	$\mathcal{J}(0.1, 10^{10})$...	Quality factor of the secondary oscillation, shared between all instruments
dQ_{GP}	$\mathcal{J}(0.1, 10^{10})$...	Difference in quality factor between the primary and secondary oscillation, shared between all instruments
$P_{\text{rot, GP}}$	$\mathcal{U}(10, 200)$	d	Period of the GP kernel, shared between all instruments
<i>QP-GP parameters</i>			
σ_{GP}	$\mathcal{J}(1, 10^6)$	ppm	Standard deviation of the GP, individual for each instrument but shared between the MEarth telescopes
α_{GP}	$\mathcal{J}(10^{-10}, 1)$...	Correlation timescale of the exponential part of the kernel, shared between all instruments
Γ_{GP}	$\mathcal{J}(0, 10)$...	Harmonic complexity of the sine part of the kernel, shared between all instruments
$P_{\text{rot, GP}}$	$\mathcal{U}(110, 120)$	d	Period of the GP kernel, shared between all instruments
<i>Instrument parameters</i>			
mflux	$\mathcal{N}(0, 0.2)$...	Median relative flux
σ	$\mathcal{J}(1, 10^6)$	ppm	A jitter added in quadrature to each instrument

Notes. The prior labels \mathcal{U} , \mathcal{J} , and \mathcal{N} represent uniform, log-uniform, and normal distributions, respectively.

Table B.2. Priors used for the RV fit of HNLiB.

Parameter	Prior	Unit	Description
<i>Planet parameters</i>			
P_b	$\mathcal{U}(30, 40)$	d	Period
K_b	$\mathcal{U}(0, 10)$	m s^{-1}	RV semi-amplitude
$t_{0,b}$ (BJD)	$\mathcal{U}(2457433, 2457450)$	d	Time of periastron passage
$\sqrt{e_b} \sin \omega_b$	$\mathcal{U}(-1.0, 1.0)$...	Parameterization for e and ω
$\sqrt{e_b} \cos \omega_b$	$\mathcal{U}(-1.0, 1.0)$...	Parameterization for e and ω
P_c	$\mathcal{U}(100, 120)$	d	Period
K_c	$\mathcal{U}(0.0, 10.0)$	m s^{-1}	RV semi-amplitude
$t_{0,c}$ (BJD)	$\mathcal{U}(2457433, 2457550)$	d	Time of periastron passage
$\sqrt{e_c} \sin \omega_c$	fixed (0)	...	Parameterization for e and ω
$\sqrt{e_c} \cos \omega_c$	fixed (0)	...	Parameterization for e and ω
<i>GP parameters</i>			
σ_{GP}	$\mathcal{U}(0.0, 10)$	m s^{-1}	Standard deviation of the GP, individual for each instrument
f_{GP}	$\mathcal{U}(0.0, 1.0)$...	Fractional amplitude of the secondary mode compared to the primary mode, shared between all instruments
$Q_{0,\text{GP}}$	$\mathcal{J}(0.1, 10^6)$...	Quality factor of the secondary oscillation, shared between all instruments
dQ_{GP}	$\mathcal{J}(0.1, 10^6)$...	Difference in quality factor between the primary and secondary oscillation, shared between all instruments
$P_{\text{rot, GP}}$	$\mathcal{N}(96, 6)$	d	Period of the GP kernel, shared between all instruments
<i>Instrument parameters</i>			
γ	$\mathcal{U}(-10, 10)$	m s^{-1}	RV zero point for CARMENES, HIRES, and HARPS
σ	$\mathcal{U}(0.0, 10)$	m s^{-1}	A jitter added in quadrature to CARMENES, HIRES, and HARPS

Notes. The prior labels \mathcal{U} , \mathcal{J} , and \mathcal{N} represent uniform, log-uniform, and normal distributions, respectively.

Table B.3. Instrumental posteriors from the final model.

Parameter	Posterior ^(a)	Units
CARMENES		
γ	$0.76^{+0.3}_{-0.3}$	m s^{-1}
σ	$0.91^{+0.31}_{-0.3}$	m s^{-1}
HARPS		
γ	$-0.8^{+1.2}_{-1.3}$	m s^{-1}
σ	$2.04^{+0.93}_{-0.7}$	m s^{-1}
HIRES		
γ	$-3.6^{+1.4}_{-1.5}$	m s^{-1}
σ	$3.4^{+1.8}_{-1.6}$	m s^{-1}

Notes. ^(a) Error bars denote the 68% posterior confidence intervals.

BID	RV [ms ⁻¹]	Ca II IRT b [Å]	He I10830 Å [Å]	Pa β [Å]	TiO λ 7048 Å [Å]	TiO λ 8428 Å [Å]	TiO λ 8838 Å [Å]	VO λ 7940 Å [Å]
2 458 533.66697	-0.7 ± 1.2	0.5755 ± 0.0017	0.0099 ± 0.0015	-0.0095 ± 0.0035	0.50282 ± 0.00085	0.8090 ± 0.0016	0.8108 ± 0.0014	0.8793 ± 0.0024
2 458 534.67050	-3.8 ± 1.1	0.5801 ± 0.0013	0.0095 ± 0.0012	-0.0081 ± 0.0036	0.50284 ± 0.00067	0.8116 ± 0.0013	0.8049 ± 0.0011	0.8798 ± 0.0019
2 458 535.68757	-4.61 ± 0.97	0.5799 ± 0.0012	0.00586 ± 0.00097	-0.0131 ± 0.0038	0.50151 ± 0.00059	0.8075 ± 0.0012	0.8026 ± 0.0010	0.8780 ± 0.0017
2 458 537.71021	-0.94 ± 0.98	0.5847 ± 0.0013	0.00667 ± 0.00092	-0.0088 ± 0.0032	0.50525 ± 0.00063	0.8100 ± 0.0012	0.7994 ± 0.0011	0.8806 ± 0.0018
2 458 542.69476	0.8 ± 1.1	0.5828 ± 0.0013	0.00894 ± 0.00083	-0.0127 ± 0.0038	0.50311 ± 0.00064	0.8091 ± 0.0012	0.7994 ± 0.0011	0.8815 ± 0.0018
2 458 543.65836	...	0.5808 ± 0.0012	0.0064 ± 0.0010	-0.0118 ± 0.0038	0.50380 ± 0.00061	0.8097 ± 0.0012	0.8073 ± 0.0010	0.8819 ± 0.0017
2 458 543.65942	...	0.5808 ± 0.0012	0.0064 ± 0.0010	-0.0118 ± 0.0038	0.50380 ± 0.00061	0.8097 ± 0.0012	0.8073 ± 0.0010	0.8819 ± 0.0017
2 458 545.65316	2.4 ± 1.2	0.5768 ± 0.0016	0.00633 ± 0.00082	-0.0105 ± 0.0035	0.50094 ± 0.00079	0.8118 ± 0.0015	0.8029 ± 0.0013	0.8794 ± 0.0022
2 458 546.65916	1.8 ± 1.0	0.5828 ± 0.0019	0.01198 ± 0.00095	-0.0095 ± 0.0034	0.49993 ± 0.00093	0.8071 ± 0.0018	0.8005 ± 0.0015	0.8782 ± 0.0026
2 458 553.72719	2.1 ± 1.1	0.5848 ± 0.0012	0.0091 ± 0.0012	-0.0050 ± 0.0042	0.49946 ± 0.00059	0.8083 ± 0.0011	0.81035 ± 0.00098	0.8776 ± 0.0016
2 458 560.73491	-1.4 ± 1.2	0.5760 ± 0.0014	0.0078 ± 0.0011	-0.0132 ± 0.0082	0.50532 ± 0.00071	0.8105 ± 0.0014	0.8085 ± 0.0012	0.8807 ± 0.0019
2 458 569.57015	3.2 ± 1.5	0.5796 ± 0.0022	0.0087 ± 0.0010	-0.0063 ± 0.0020	0.5022 ± 0.0011	0.8099 ± 0.0021	0.8020 ± 0.0018	0.8769 ± 0.0030
2 458 603.48060	-0.5 ± 1.2	0.5833 ± 0.0012	0.00929 ± 0.00081	-0.0075 ± 0.0017	0.50249 ± 0.00058	0.8057 ± 0.0011	0.8130 ± 0.0010	0.8808 ± 0.0016
2 458 604.52155	-0.06 ± 0.96	0.5816 ± 0.0012	0.00773 ± 0.00082	-0.0047 ± 0.0011	0.50048 ± 0.00061	0.8052 ± 0.0011	0.8125 ± 0.0010	0.8805 ± 0.0017
2 458 605.57208	0.49 ± 0.94	0.5805 ± 0.0012	0.00772 ± 0.00096	0.00646 ± 0.00068	0.50332 ± 0.00060	0.8044 ± 0.0011	0.8088 ± 0.0010	0.8834 ± 0.0017
2 458 610.51896	1.8 ± 1.2	0.5840 ± 0.0013	0.00995 ± 0.00078	-0.00457 ± 0.00074	0.50280 ± 0.00065	0.8071 ± 0.0012	0.8068 ± 0.0011	0.8820 ± 0.0018
2 458 614.48521	1.5 ± 1.0	0.5825 ± 0.0013	0.00741 ± 0.00090	-0.00349 ± 0.00068	0.50194 ± 0.00063	0.8095 ± 0.0012	0.8123 ± 0.0011	0.8814 ± 0.0017
2 458 619.54597	3.0 ± 1.1	0.5833 ± 0.0012	0.00843 ± 0.00078	-0.0044 ± 0.00078	0.50248 ± 0.00060	0.8051 ± 0.0011	0.81619 ± 0.00100	0.8814 ± 0.0016
2 458 646.41563	-2.9 ± 1.9	0.5791 ± 0.0021	0.0047 ± 0.0011	0.00443 ± 0.00074	0.4976 ± 0.0011	0.8008 ± 0.0019	0.8270 ± 0.0017	0.8850 ± 0.0028
2 458 647.42417	-1.3 ± 1.2	0.5879 ± 0.0013	0.0158 ± 0.0019	0.0012 ± 0.0012	0.49784 ± 0.00063	0.8011 ± 0.0012	0.8347 ± 0.0011	0.8760 ± 0.0017
2 458 657.40840	1.0 ± 1.3	0.5873 ± 0.0013	0.00810 ± 0.00086	0.00646 ± 0.00068	0.49473 ± 0.00062	0.8033 ± 0.0011	0.8401 ± 0.0011	0.8782 ± 0.0017
2 458 661.42292	1.8 ± 1.7	0.5871 ± 0.0021	-0.0457 ± 0.0010	-0.0003 ± 0.0100	0.4938 ± 0.0011	0.7993 ± 0.0019	0.8390 ± 0.0018	0.8814 ± 0.0029
2 458 662.44232	1.5 ± 1.9	0.5823 ± 0.0028	-0.1002 ± 0.0013	0.0059 ± 0.0010	0.4938 ± 0.0014	0.7963 ± 0.0025	0.8416 ± 0.0023	0.8705 ± 0.0036
2 458 681.37492	0.9 ± 1.0	0.5829 ± 0.0014	-0.06744 ± 0.00088	-0.00273 ± 0.00088	0.49371 ± 0.00066	0.8086 ± 0.0017	0.8428 ± 0.0016	0.8788 ± 0.0018
2 458 691.36881	3.6 ± 1.2	0.5835 ± 0.0018	-0.0728 ± 0.0010	-0.00606 ± 0.00084	0.49101 ± 0.00089	0.8086 ± 0.0017	0.8428 ± 0.0016	0.8778 ± 0.0024
2 458 865.74522	4.7 ± 2.2	0.5760 ± 0.0039	-0.0128 ± 0.0018	-0.0071 ± 0.0028	0.5024 ± 0.0020	0.8049 ± 0.0037	0.8093 ± 0.0031	0.8712 ± 0.0053
2 458 877.74747	-3.1 ± 1.5	0.5745 ± 0.0013	-0.0004 ± 0.0014	-0.0120 ± 0.0036	0.49933 ± 0.00066	0.8072 ± 0.0013	0.8048 ± 0.0011	0.8761 ± 0.0018
2 458 881.73734	...	0.589 ± 0.018	0.5114 ± 0.0087	0.797 ± 0.016	0.808 ± 0.012	0.868 ± 0.019
2 458 885.74379	-4.7 ± 1.2	0.5720 ± 0.0014	0.00005 ± 0.00091	-0.0102 ± 0.0035	0.50364 ± 0.00068	0.8112 ± 0.0013	0.8034 ± 0.0012	0.8794 ± 0.0019
2 458 889.72751	-8.0 ± 1.3	0.5763 ± 0.0014	-0.0047 ± 0.0014	-0.0093 ± 0.0036	0.50339 ± 0.00070	0.8111 ± 0.0013	0.8048 ± 0.0012	0.8811 ± 0.0020
2 458 895.74796	-5.9 ± 1.0	0.5709 ± 0.0013	0.00168 ± 0.00097	-0.0148 ± 0.0037	0.50604 ± 0.00063	0.8108 ± 0.0012	0.8071 ± 0.0011	0.8817 ± 0.0018
2 458 903.67784	-0.4 ± 1.1	0.5796 ± 0.0012	0.00446 ± 0.00075	-0.0128 ± 0.0038	0.50339 ± 0.00060	0.8090 ± 0.0012	0.8037 ± 0.0010	0.8813 ± 0.0017
2 458 913.64500	1.1 ± 1.1	0.5830 ± 0.0014	0.00979 ± 0.00073	-0.0092 ± 0.0036	0.50364 ± 0.00071	0.8120 ± 0.0014	0.8052 ± 0.0012	0.8831 ± 0.0020
2 458 917.69630	1.4 ± 1.4	0.5868 ± 0.0021	0.00156 ± 0.00096	-0.0046 ± 0.0033	0.5011 ± 0.0011	0.8111 ± 0.0020	0.8089 ± 0.0017	0.8771 ± 0.0029
2 458 923.67628	0.1 ± 1.1	0.5770 ± 0.0014	0.01119 ± 0.00075	-0.0063 ± 0.0034	0.50112 ± 0.00067	0.8102 ± 0.0013	0.8069 ± 0.0012	0.8765 ± 0.0019
2 458 982.55918	1.0 ± 1.5	0.5879 ± 0.0020	0.0012 ± 0.0033	-0.0067 ± 0.0014	0.5014 ± 0.0010	0.8055 ± 0.0019	0.8078 ± 0.0017	0.8782 ± 0.0028
2 458 989.46752	-4.0 ± 1.2	0.5835 ± 0.0014	0.0040 ± 0.0015	-0.0069 ± 0.0012	0.50080 ± 0.00070	0.8021 ± 0.0013	0.8197 ± 0.0012	0.8806 ± 0.0019
2 458 999.43482	-4.3 ± 1.3	0.5879 ± 0.0012	0.01061 ± 0.00097	-0.00391 ± 0.00065	0.50114 ± 0.00059	0.8036 ± 0.0011	0.8289 ± 0.0010	0.8808 ± 0.0016
2 459 006.47245	-3.2 ± 2.0	0.5833 ± 0.0026	0.00551 ± 0.00090	0.0004 ± 0.0010	0.5161 ± 0.0013	0.8045 ± 0.0024	0.8310 ± 0.0022	0.8819 ± 0.0034
2 459 012.39093	5.1 ± 2.0	0.5822 ± 0.0027	0.0052 ± 0.0013	-0.00275 ± 0.00088	0.4953 ± 0.0013	0.8008 ± 0.0024	0.8388 ± 0.0022	0.8740 ± 0.0036
2 459 024.42111	4.5 ± 1.8	0.5861 ± 0.0016	-0.0125 ± 0.0024	0.0044 ± 0.0011	0.49497 ± 0.00081	0.8032 ± 0.0015	0.8401 ± 0.0014	0.8812 ± 0.0023
2 459 036.39359	1.3 ± 1.3	0.5938 ± 0.0016	-0.04560 ± 0.00090	0.00182 ± 0.00076	0.49283 ± 0.00076	0.8057 ± 0.0014	0.8360 ± 0.0013	0.8724 ± 0.0020
2 459 053.37775	...	0.5910 ± 0.0018	-0.0569 ± 0.0011	-0.00359 ± 0.00093	0.48490 ± 0.00082	0.8038 ± 0.0016	0.8453 ± 0.0015	0.8787 ± 0.0023
2 459 053.37782	...	0.5910 ± 0.0018	-0.0569 ± 0.0011	-0.00359 ± 0.00093	0.48490 ± 0.00082	0.8038 ± 0.0016	0.8453 ± 0.0015	0.8787 ± 0.0023
2 459 061.35479	10.6 ± 1.5	0.5912 ± 0.0018	-0.1054 ± 0.0012	-0.000226 ± 0.00084	0.48722 ± 0.00089	0.8002 ± 0.0017	0.8406 ± 0.0016	0.8796 ± 0.0024
2 459 214.76769	-7.0 ± 1.5	0.5838 ± 0.0015	0.00374 ± 0.00081	-0.0126 ± 0.0042	0.50741 ± 0.00076	0.8095 ± 0.0014	0.8044 ± 0.0013	0.8811 ± 0.0021